J. Fluid Mech. (1999), *vol.* 384, *pp.* 207–241. Printed in the United Kingdom

The mechanism of vortex connection at a free surface

By CHIONG ZHANG, LIAN SHEN AND DICK K. P. YUE†

Department of Ocean Engineering, Massachusetts Institute of Technology, Cambridge, MA 02139, USA

(Received 10 June 1998 and in revised form 11 November 1998)

Vortex connections at the surface are fundamental and prominent features in free-surface vortical flows. To understand the detailed mechanism of such connection, we consider, as a canonical problem, the laminar vortex connections at a free surface when an oblique vortex ring impinges upon that surface. We perform numerical simulations of the Navier–Stokes equations with viscous free-surface boundary conditions. It is found that the key to understanding the mechanism of vortex connection at a free surface is the surface layers: a viscous layer resulting from the dynamic zero-stress boundary conditions at the free surface, and a thicker blockage layer which is due to the kinematic boundary condition at the surface. In the blockage layer, the vertical vorticity component increases due to vortex stretching and vortex turning (from the transverse vorticity component). The vertical vorticity is then transported to the free surface through viscous diffusion and vortex stretching in the viscous layer leading to increased surface-normal vorticity. These mechanisms take place at the aft-shoulder regions of the vortex ring. Connection at the free surface is different from that at a free-slip wall owing to the generation of surface secondary vorticity. We study the components of this surface vorticity in detail and find that the presence of a free surface accelerates the connection process. We investigate the connection time scale and its dependence on initial incidence angle, Froude and Reynolds numbers. It is found that a criterion based on the streamline topology provides a precise definition for connection time, and may be preferred over existing definitions, e.g. those based on free-surface elevation or net circulation.

1. Introduction

For vortical flows near a free surface, an important interaction mechanism is that vortex lines may disconnect and subsequently terminate at the free surface resulting in persistent normal vorticity on the free surface (Bernal & Kwon 1989). Such vortex connection phenomena are a result of three-dimensional vortex dynamics and viscous effects. It turns out that vortex connection is fundamental to viscous flows involving free surfaces and plays an important role in a large variety of free-surface flows such as ocean turbulence, breaking waves and ship wakes (Kasischke, Meadows & Jackson 1984; Sarpkaya 1996).

According to the Helmholtz theorem, a vortex filament cannot begin or end within a fluid. Nevertheless, mechanisms which may allow the filament to (disconnect and then) reconnect at a boundary are not precluded. If the fluid is inviscid, however, Kelvin's circulation theorem requires the vortex filament to move as a material filament and

† Author to whom correspondence should be addressed.

hence it cannot be broken in the fluid. Thus vortex reconnection at a boundary must be an inherently viscous phenomenon. Kambe (1984) showed that for two oppositely signed vortex systems in a two-dimensional straining field, the cancellation of vorticity has a critical time scale proportional to a logarithm of the Reynolds number for fixed strain rate. Using a viscosity-driven model, Saffman (1990) obtained a set of model equations to describe the reconnection of two two-dimensional counter-rotating vortex cores in close proximity. He provided preliminary numerical results together with connection time scales predicted by the model. Shelley, Meiron & Orszag (1993) later showed that the asymptotic behaviour of Saffman's model can be understood completely in terms of the behaviour of special solutions of the model equations, which lead to a time scale for the reconnection similar to that of Kambe (1984). Numerical simulations of vortex reconnections provide additional insight into this problem. Kida, Takaoka & Hussain (1991) performed direct Navier–Stokes equations simulation of the laminar collision and subsequent connection of two identical vortex rings. They showed that the mechanism of connection is that of *bridging* (Melander & Hussain 1990) and that the location of initial connection is close to the position of maximum strain rate.

Vortex connection at a free surface is often considered to be analogous to two-vortex reconnections in that the latter is the zero-Froude-number limit (i.e. the free-slip wall case) of the former. The two problems are, however, dynamically different in that on a free surface constant pressure obtains, while on a free-slip wall tangential pressure gradients play a role. In the presence of a free surface, the connection mechanism is also more complicated since the free surface can deform and generate (secondary) surface vorticity which has a significant effect on the overall connection process. According to Batchelor (1967), the surface vorticity in two-dimensional flow is equal to twice the tangential surface velocity multiplied by the surface curvature, which has been shown experimentally (e.g. Sarpkaya & Suthon 1990). Recently, Longuet-Higgins (1998) pointed out that in three-dimensional flow, in addition to a component of vorticity perpendicular to the flow there is also a component parallel to the direction of flow.

A particularly useful yet simple model for understanding free-surface vortex connection is the canonical problem of a vortex ring approaching and connecting to a free surface. For this problem, the relevant length scale is the ring radius R, the velocity scale is then $U = \Gamma_0/R$, where Γ_0 is the (initial) velocity circulation of the ring. Based on these scales, the parameters characterizing this problem are Reynolds number $R_e = \Gamma_0/\nu$, where ν is the kinematic viscosity, and Froude number $F_r = \Gamma_0/g^{1/2}R^{3/2}$, where g is the acceleration due to gravity. (Although surface contamination can have important effects on the vortical free-surface interactions, e.g. Bernal *et al.* 1989, Tsai & Yue 1995, for simplicity, surface tension and surfactant effects are not considered here.)

This vortex ring connection problem has been a subject of experimental investigation. Bernal & Kwon (1989) performed the first clear flow visualization study of vortex ring connection to a free surface. Recently, Gharib *et al.* (1992), Gharib & Weigand (1996) reconsidered the problem and provided quantitative measurements of the surface and centre-plane vorticity using digital particle image velocimetry to show the role of the surface secondary vorticity.

Motivated largely by the experimental studies, free-surface vortex connections have also been studied numerically. Dommermuth & Yue (1990) and Dommermuth (1993) performed laminar-flow simulations of a sinusoidally perturbed vortex tube moving parallel to a free surface and showed that the generation of helical vorticity plays a

role in the vortex breakdown leading to subsequent surface connection. This problem was also studied experimentally by Willert & Gharib (1997). Simulations for the case of a ring approaching a deformable surface were performed by Lugt & Ohring (1994) and Ohring & Lugt (1996). These simulations provide a more complete picture of the process of free-surface vortex connection.

While vortex connections at a free surface have been observed experimentally and in simulations, detailed mechanism of the connection processes has not been fully obtained. In this work, we study the mechanism of laminar vortex ring connection at a free surface by direct simulation of the Navier–Stokes equations with full viscous, free-surface boundary conditions. For simplicity, we consider relatively small Froude numbers for which linearized free-surface boundary conditions apply. The main goals of this study are: (i) to elucidate the detailed mechanism of the vortex connection process in terms of the vorticity structures, evolutions and transformations near the free surface; (ii) to understand the role of the free surface in the connection process; and (iii) to identify/quantify the vortex connection time and its dependence on the initial incidence angle, Froude and Reynolds numbers.

The rest of the paper is organized as follows. In § 2 we provide the mathematical formulation that describes the viscous interaction of a vortex ring with a free surface; and in § 3 we discuss its numerical implementation. We present the simulation results in § 4. We first elucidate the general features of vortex ring connection to a free surface. The detailed mechanism for the vortex connection is then investigated in terms of near-surface vorticity evolutions and transformations and the role of the surface layers. We finally consider the question of connection time (based on free-surface streamline topology) and study its dependence on the initial incidence angle, and Froude and Reynolds numbers of the ring. In § 5, we make some concluding remarks. A brief discussion of the relationship between the instantaneous free-surface elevation and surface-normal vorticity is included in an Appendix.

2. Mathematical formulation

2.1. *Field equations*

We consider the unsteady incompressible viscous flow of a Newtonian fluid under a free surface. Referring to figure 1 for the vortex ring, the vertical coordinate $z = x_3$ is positive upward, and $z = 0$ coincides with the undisturbed free surface. For simplicity, we choose physical units so that the (initial) ring radius R, the (initial) circulation of the ring Γ_0, and fluid density ρ are unity. All subsequent variables are normalized accordingly unless otherwise stated. For an isotropic and homogeneous fluid, the normalized Navier–Stokes equations for conservation of momentum have the form

$$\frac{\partial u_i}{\partial t} + \frac{\partial}{\partial x_j} u_i u_j = -\frac{\partial p}{\partial x_j} + \frac{1}{R_e} \frac{\partial^2 u_i}{\partial x_j \partial x_j}, \tag{2.1}$$

where $\boldsymbol{v} = \{u_i\}$ is the velocity, and p is the hydrodynamic pressure which is related to the total pressure P by

$$p = P + \frac{1}{F_r^2} z.$$

The Navier–Stokes equations (2.1) must be solved together with the continuity

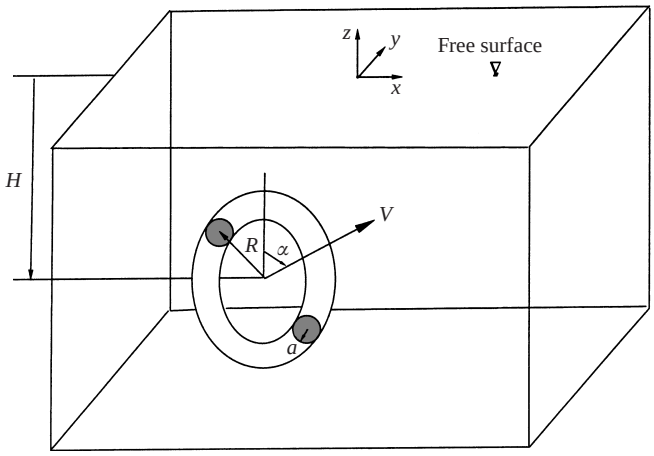

FIGURE 1. Domain of computation and coordinate system.

equation

$$\frac{\partial u_i}{\partial x_i} = 0. \tag{2.2}$$

2.2. *Free-surface boundary conditions*

We derive the boundary conditions at the free surface. Let the free-surface elevation be given by $\eta(x, y, t)$. The fact that no fluid particle leaves the free surface gives the kinematic boundary condition

$$\eta_t + u\eta_x + v\eta_y - w = 0 \quad \text{on} \quad z = \eta. \tag{2.3}$$

Before the dynamic boundary conditions can be obtained, we first write down the total stress tensor $\boldsymbol{\sigma}$ in matrix form:

$$\boldsymbol{\sigma} = \begin{bmatrix} -P + 2u_x/R_e & (u_y + v_x)/R_e & (u_z + w_x)/R_e \\ (v_x + u_y)/R_e & -P + 2v_y/R_e & (v_z + w_y)/R_e \\ (w_x + u_z)/R_e & (w_y + v_z)/R_e & -P + 2w_z/R_e \end{bmatrix}. \tag{2.4}$$

The directional unit vectors on the free surface can be expressed in terms of η:

$$\left.\begin{aligned} \boldsymbol{n} &= \frac{\{-\eta_x, -\eta_y, 1\}}{(\eta_x^2 + \eta_y^2 + 1)^{1/2}} \\ \boldsymbol{t}_1 &= \frac{\{1, 0, \eta_x\}}{(\eta_x^2 + 1)^{1/2}} \\ \boldsymbol{t}_2 &= \frac{\{0, 1, \eta_y\}}{(\eta_y^2 + 1)^{1/2}} \end{aligned}\right\} \quad \text{on} \quad z = \eta, \tag{2.5}$$

where $\{n\}$ is the unit vector normal to the free surface, and $\{t_1\}$ and $\{t_2\}$ are unit tangent vectors in the (x, z)- and (y, z)-planes respectively.

Neglecting surface tension and external stresses, the balance of (two) tangential and (one) normal stress components on the free surface gives

$$\left.\begin{aligned} \boldsymbol{t}_1 \cdot \boldsymbol{\sigma} \cdot \boldsymbol{n}^T &= 0 \\ \boldsymbol{t}_2 \cdot \boldsymbol{\sigma} \cdot \boldsymbol{n}^T &= 0 \\ \boldsymbol{n} \cdot \boldsymbol{\sigma} \cdot \boldsymbol{n}^T &= 0 \end{aligned}\right\} \quad \text{on} \quad z = \eta. \tag{2.6}$$

Substituting (2.4) and (2.5) into (2.6) yields the corresponding dynamic boundary conditions on the free surface in terms of velocity and η:

$$2\eta_x(w_z - u_x) - \eta_y(u_y + v_x) + (1 - \eta_x^2)(u_z + w_x) - \eta_x\eta_y(v_z + w_y) = 0 \quad \text{on} \quad z = \eta, \tag{2.7}$$

$$2\eta_y(w_z - v_y) - \eta_x(u_y + v_x) + (1 - \eta_y^2)(v_z + w_y) - \eta_x\eta_y(u_z + w_x) = 0 \quad \text{on} \quad z = \eta, \tag{2.8}$$

$$\frac{\eta}{F_r^2} - p + \frac{2}{R_e(1 + \eta_x^2 + \eta_y^2)}(\eta_x^2 u_x + \eta_x\eta_y(u_y + v_x) + \eta_y^2 v_y - \eta_x(u_z + w_x) - \eta_y(v_z + w_y) + w_z) = 0 \quad \text{on} \quad z = \eta. \tag{2.9}$$

We consider moderate to small Froude numbers so that the free-surface boundary conditions (2.3), (2.7), (2.8) and (2.9) can be linearized. Assuming $\eta = O(\varepsilon) \ll 1$, we expand the conditions on the undisturbed free surface $z = 0$ and obtain, to leading order of ε,

$$\eta_t + (u\eta)_x + (v\eta)_y - w = 0 + O(\varepsilon^2), \tag{2.10}$$

$$2\eta_x(w_z - u_x) - \eta_y(u_y + v_x) + u_z + w_x - \eta(u_{xx} - u_{zz} + v_{xy}) = 0 + O(\varepsilon^2), \tag{2.11}$$

$$2\eta_y(w_z - v_y) - \eta_x(u_y + v_x) + v_z + w_y - \eta(u_{xy} + v_{yy} - v_{zz}) = 0 + O(\varepsilon^2), \tag{2.12}$$

$$p = \frac{1}{F_r^2}\eta + \frac{2}{R_e}w_z + O(\varepsilon^2). \tag{2.13}$$

These free-surface boundary conditions ((2.10)–(2.13)) are used in the present study.

If $z = 0$ is a free-slip wall, the tangential stresses, normal velocity and normal pressure gradient are zero there, and the appropriate boundary conditions on $z = 0$ are: $u_z = v_z = w = p_z = 0$. These conditions are recovered from (2.10)–(2.13) as a limiting case. Setting $F_r = 0$ in (2.13), we obtain $\eta = 0$. Elimination of η from (2.10) leads to $w = 0$. Therefore, (2.11) and (2.12) can be written as $u_z = 0$ and $v_z = 0$. With these conditions, $p_z = 0$ is obtained from (2.1), and thus the case of a free-slip wall is the $F_r = 0$ limit of the present problem.

2.3. *Surface vorticity*

The vorticity at the free surface plays an important role in the connection process, and differs substantially from that for the free-slip wall. Let the vorticity be denoted by $\boldsymbol{\omega} = (\omega_x \equiv w_y - v_z, \omega_y \equiv u_z - w_x, \omega_z \equiv v_x - u_y)$, and the surface vorticity defined as $\boldsymbol{\omega}^s \equiv (\omega_x, \omega_y)|_{z=\eta}$. The general expression for $\boldsymbol{\omega}^s$ in terms of the relevant surface parameters, i.e. surface tangential velocities u, v and elevation η, is quite involved for the fully nonlinear case. Consistent with the linearization of § 2.2, we seek the appropriate results to leading order in terms of $O(\varepsilon)$.

Using the free-surface dynamic conditions (2.7) and (2.8), we obtain

$$\left.\begin{aligned} \omega_x^s &= 2w_y - 2\eta_y(v_y - w_z) - \eta_x(u_y + v_x) + O(\varepsilon^2) \\ \omega_y^s &= -2w_x + 2\eta_x(u_x - w_z) + \eta_y(u_y + v_x) + O(\varepsilon^2) \end{aligned}\right\} \quad \text{on} \quad z = \eta. \tag{2.14}$$

We now expand (2.14) on $z = 0$:

$$\left.\begin{aligned} \omega_x^s &= 2w_y + 2\eta w_{yz} - 2\eta_y(v_y - w_z) - \eta_x(u_y + v_x) + O(\varepsilon^2) \\ \omega_y^s &= -2w_x - 2\eta w_{xz} + 2\eta_x(u_x - w_z) + \eta_y(u_y + v_x) + O(\varepsilon^2) \end{aligned}\right\} \quad \text{on} \quad z = 0. \tag{2.15}$$

Using the continuity equation (2.2), we express w_z in terms of u_x and v_y in (2.15),

and apply the kinematic boundary condition (2.10) on $z = 0$ to eliminate w to finally obtain linearized forms of the surface tangential vorticity:

$$\omega_x^s = 2\eta_{yt} + 2\eta_{xy}u + 2\eta_{yy}v + \eta_x u_y - \eta_x v_x + O(\varepsilon^2) \qquad \text{on} \quad z = 0, \tag{2.16}$$

$$\omega_y^s = -2\eta_{xt} - 2\eta_{xy}v - 2\eta_{xx}u + \eta_y u_y - \eta_y v_x + O(\varepsilon^2) \qquad \text{on} \quad z = 0. \tag{2.17}$$

Note that $\boldsymbol{\omega}^s$ is defined on $z = \eta$ only; the right-hand sides of (2.14) are evaluated at $z = \eta$; while the right-hand sides of (2.15)–(2.17) are evaluated at $z = 0$.

The present expression for the surface vorticity components (2.16) and (2.17) are extensions of existing formulations. Batchelor (1967) and Lugt (1987) considered the surface vorticity in steady two-dimensional flow, which corresponds to (2.16) and (2.17) with only the third terms on the right-hand sides. Lundgren (1988) and Gharib (1994) analysed the unsteady two-dimensional case, which corresponds to the first terms on the right-hand sides of (2.16) and (2.17). Recently, Longuet-Higgins (1998) pointed out that for steady three-dimensional flow, there exists a vorticity component parallel to the direction of flow. This steady three-dimensional effect corresponds directly with the second, fourth, and fifth terms in (2.16) and (2.17) in the present Cartesian coordinates.

2.4. *Conservation of energy*

Multiplying (2.1) by u_i and integrating over a finite volume V enclosed by boundary S, we obtain the equation for the evolution of the total kinetic energy:

$$\frac{\mathrm{d}}{\mathrm{d}t}\iiint_V \frac{u_i u_i}{2}\mathrm{d}V = \iint_S n_j u_i \left[-p\delta_{ij} + \frac{1}{R_e}\left(\frac{\partial u_i}{\partial x_j} + \frac{\partial u_j}{\partial x_i}\right)\right]\mathrm{d}S - \frac{1}{R_e}\iiint_V \left(\frac{\partial u_i}{\partial x_j} + \frac{\partial u_j}{\partial x_i}\right)\frac{\partial u_i}{\partial x_j}\mathrm{d}V. \tag{2.18}$$

Upon substitution of the free-surface boundary conditions (2.10)–(2.13), we obtain

$$\frac{\mathrm{d}}{\mathrm{d}t}\iiint_V \frac{u_i u_i}{2}\mathrm{d}V = -\frac{1}{2F_r^2}\frac{\mathrm{d}}{\mathrm{d}t}\iint_{S_f}\eta^2\mathrm{d}S - \frac{1}{R_e}\iiint_V \left(\frac{\partial u_i}{\partial x_j} + \frac{\partial u_j}{\partial x_i}\right)\frac{\partial u_i}{\partial x_j}\mathrm{d}V, \tag{2.19}$$

where S_f is the projection of the free surface onto the (x, y)-plane, and we have assumed that there is no net contribution to (2.18) from the remaining portions of S. The energy conservation (2.19) is checked and conserved in all our numerical results to within $O(1)\%$.

3. Numerical method

3.1. *Numerical scheme*

In this paper, the three-dimensional Navier–Stokes equations (2.1) and the continuity equation (2.2) combined with the free-surface boundary conditions (2.10)–(2.13) are solved numerically as an initial-boundary-value problem. The computational domain is closed by imposing periodic conditions on the four vertical boundaries far away, and by a free-surface boundary on the top and a free-slip boundary on the bottom. Spectral and second-order finite-difference discretizations are used in the horizontal and vertical dimensions respectively. A second-order Runge–Kutta scheme is used for time integration. We use a projection method which couples the continuity equation with the momentum equations to obtain a Poisson equation with a divergence correction for the pressure. The Poisson equation for the pressure is solved at each sub

time step. In order to maintain continuity in the numerical sense, the Poisson equation is solved using two grid systems – a regular grid and a staggered grid shifted in the vertical direction by half a grid spacing. The vertical velocity (w) is assigned on the staggered grid while all other variables (u, v and p) are assigned on the regular grid. Among the free-surface boundary conditions, the normal-stress condition (2.13) is used as Dirichlet condition for the Poisson equation; the tangential-stress conditions (2.11) and (2.12) are used to evaluate the z-derivatives of horizontal velocities in (2.1) at the free surface; and the kinematic condition (2.10) is used to update the free-surface elevation. Details of the numerical implementation can be found in Zhang (1996).

3.2. *Initial conditions*

The initial set-up of the vortex ring is shown in figure 1. The distance between the centre of the ring and the undisturbed free surface is H. The radius of the vortex ring is R and the vortex core radius is a. The generating axis of the vortex ring is in the direction of advection of the ring which makes an angle α measured from the $+z$-axis. ($\alpha = 90^\circ$ for a ring traveling parallel to the $+x$-axis.)

To specify the initial vorticity field of the vortex ring, we use a Gaussian core distribution, which satisfies Navier–Stokes equations for viscous flow (Lamb 1932):

$$\omega = \omega_c \exp\left(-\frac{(x-x_0)^2 + (y-y_0)^2 + (z-z_0)^2}{a^2}\right), \tag{3.1}$$

where ω_c is the (initial) maximum core vorticity and (x_0, y_0, z_0) is the centre of the core which in this case corresponds to a circle at the ring geometric centre. Note that the circular symmetric (3.1) in general obtains for small a/R. For the present study, $a/R = 0.35$ (see table 2) and the initial core distribution is expected to change slightly after the simulation is started.

Given the initial vorticity distribution $\boldsymbol{\omega}$, the velocity field required to start the numerical simulation can be obtained in terms of the vector stream function $\boldsymbol{\psi}$ defined by $\boldsymbol{V} = \nabla \times \boldsymbol{\psi}$. The velocity is obtained after solving the Poisson equation governing $\boldsymbol{\psi}$:

$$\nabla^2 \boldsymbol{\psi} = -\boldsymbol{\omega}. \tag{3.2}$$

3.3. *Validation and convergence tests*

We perform a number of tests to establish the accuracy and convergence of our numerical method. We first consider two problems for which analytic solutions exist: the translation and diffusion of a Lamb vortex filament placed asymmetrically in a cubic domain, and the surface vorticity associated with a viscous three-dimensional standing wave. We then perform convergence tests for the vortex ring problem itself and also compare the results to experimental measurements.

3.3.1. *Decay of a Lamb vortex filament*

Since the free decay of a Lamb vortex in an unbounded domain does not involve the nonlinear convective terms, we consider instead a vortex filament placed asymmetrically inside a cubic periodic domain. Free-slip conditions are applied on the boundaries at the top and the bottom. Because of the presence of the 'image' vortices, the vortex filament orbits within the box. For small core sizes relative to the dimension of the domain, however, the core vorticity should still decay at a rate close to that in an unbounded domain.

Figure 2 shows the convergence of the core vorticity value (at $t = 16$) with grid size

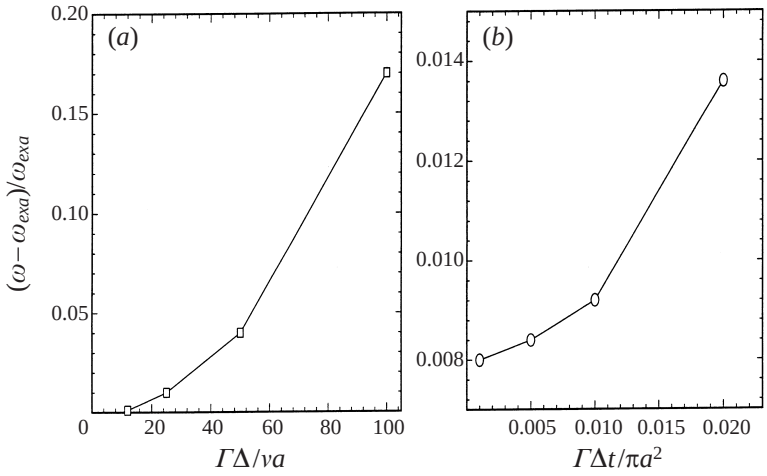

FIGURE 2. Relative error of maximum vorticity $|\omega_{\max} - \omega_{exa}|/\omega_{exa}$ at $t = 16$ for a decaying Lamb vortex filament in a cubic box as a function of: (*a*) grid Reynolds number $\Gamma\Delta/va$ with fixed normalized time step $\delta t\Gamma/\pi a^2 = 0.005$; and (*b*) normalized time step $\delta t\Gamma/\pi a^2$ with fixed grid Reynolds number $\Delta\Gamma/va = 12.5$.

and time step respectively. Here, $\omega_{\max}$ is the computed maximum core vorticity value and $\omega_{exa} = 1/(a^2 + 4\nu t)$ the analytic unbounded domain solution. The parameters for this case are: initial circulation of the Lamb vortex $\Gamma_0 = \pi$; initial core radius $a = 0.25$; and equal grid spacing $\Delta x = \Delta y = \Delta z = \Delta$.

3.3.2. *Viscous three-dimensional standing wave*

To verify the treatment of the free-surface boundary conditions, we consider a three-dimensional standing wave of a viscous fluid, where, for small wave amplitude, the free-surface elevation η is obtained in closed form (Lamb 1932):

$$\eta = a\cos(\sigma t)\exp(-2\nu\kappa^2 t)\cos(k_x x)\cos(k_y y) = A(t)\cos(k_x x)\cos(k_y y). \tag{3.3}$$

Here k_x, k_y are the wavenumbers along the x- and y-axes respectively, $\kappa^2 = k_x^2 + k_y^2$, and the wave frequency σ is given by the dispersion relation, $\sigma^2 = \kappa g$, for large fluid depth.

To be specific, we consider a case with $F_r = a\sigma/(g/\kappa)^{1/2} = 1/(2\pi)$ and $R_e = a\sigma/\kappa\nu = 500$, and compare our computational results to (3.3) after one wave period $2\pi/\sigma$. Table 1 shows the relative errors in the wave amplitude, A, and the surface vorticity $\boldsymbol{\omega}^s$ (see (2.16) and (2.17)), for different space and time discretization. The numerical scheme predicts well the attenuation of the wave amplitude and surface vorticity.

3.3.3. *Vortex ring connection*

We finally consider the subject problem of the connection of a vortex ring at a free surface. The physical parameters of the cases we study in this paper are listed in table 2. We show here the convergence results for Case II using 64^3 and 128^3 grid points respectively. Figure 3(*a*) shows the time evolution of the maximum transverse vorticity $\omega_{y\max}$ (of the upper limb of the ring) on the symmetry plane $y = 0$ and maximum vertical vorticity $\omega_{z\max}$ on the free surface $z = 0$. The results are clearly grid independent. Similar convergence for the evolution of the surface wave energy $\int\int_{S_f} \eta^2 \mathrm{d}S/F_r^2$ is also obtained and is plotted in figure 3(*b*).

Δ/λ	$\delta t\ \sigma/2\pi$	ε_A	ε_ω
0.01	0.01	0.0031	0.015
0.008	0.01	0.0014	0.010
0.008	0.002	0.0012	0.006
0.008	0.001	0.0011	0.005

TABLE 1. Relative errors in the wave amplitude $\varepsilon_A = |A - A_{exa}|/A_{exa}$ and surface vorticity $\varepsilon_\omega = \max(|\boldsymbol{\omega}^s - \boldsymbol{\omega}^s_{exa}|)/\max(|\boldsymbol{\omega}^s_{exa}|)$, at time $t = 2\pi/\sigma$ for the attenuation of a viscous three-dimensional standing wave as a function of grid size Δ and time step δt.

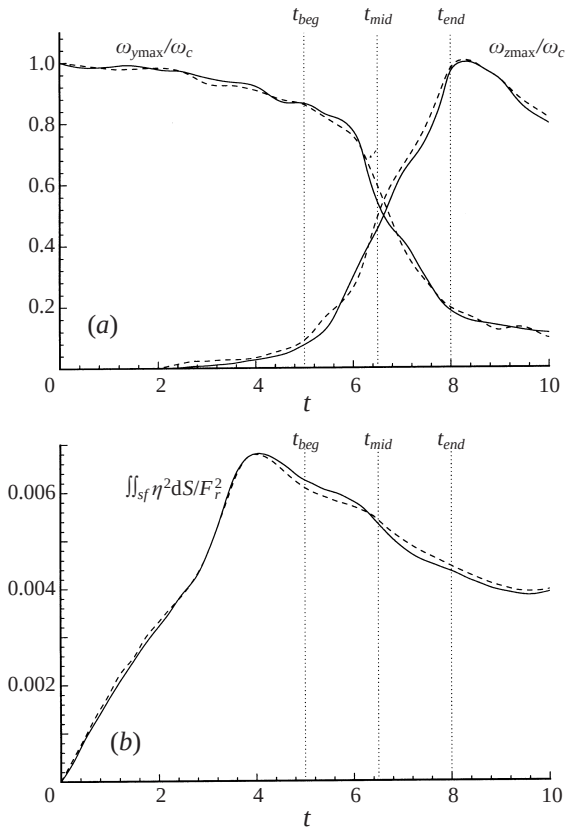

FIGURE 3. Time evolution of (*a*) the maximum transverse vorticity on $y = 0$, $\omega_{y\max}$, and maximum vertical vorticity on $z = 0$, $\omega_{z\max}$; and (*b*) total surface wave energy for the vortex connection at a free surface corresponding to Case II of table 2. The results shown are for simulations obtained using: ———— , 128^3 grid points; and – – – – , 64^3 grid points.

In all subsequent computations, we use 128^3 grid points with $\delta t = 0.005$. The conservation of total energy according to (2.18) is within $O(1)\%$ error and the maximum mass divergence at any grid points is less than 10^{-14} for all the simulations.

As a final validation, we compare our numerical predictions to experimental measurements. Figure 4 shows such a comparison for the evolution of $\omega_{y\max}$ and $\omega_{z\max}$ during the connection process for the case studied experimentally by M. Gharib (1992, personal communication), with the computations and experiments using iden-

Case	R_e	F_r	α (deg.)	H	T_ψ	T_Γ
I	1570	0.00	80	1.57	2.61	2.56
II	1570	0.47	80	1.57	2.49	2.58
III	1570	0.47	70	1.875	5.20	3.20
IV	1570	0.47	60	1.875	7.38	3.41
V	942	0.47	60	1.875	6.08	3.74
VI	471	0.47	60	1.875	4.09	5.11

TABLE 2. Physical parameters used in the different simulations (all based on the initial circulation of the vortex ring $\Gamma_0 \equiv 1$ and the ring radius $R \equiv 1$). The connection times based on streamline topology T_ψ and on velocity circulation T_Γ are also given for each case. The rings have an initial core radius $a = 0.35$. The computational domain size is $8 \times 8 \times 4$, a 128^3 grid is used, and the time step is $\delta t = 0.005$.

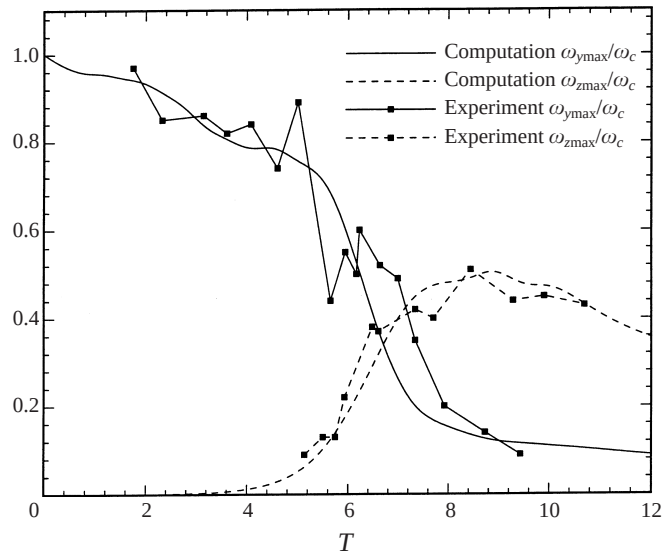

FIGURE 4. Comparison between experiments (Gharib 1992, personal communication) and computations of the time evolution of the maximum transverse vorticity on $y = 0$, $\omega_{y\max}$, and maximum vertical vorticity on $z = 0$, $\omega_{z\max}$ during the connection of a vortex ring at a free surface. The physical parameters are: $R_e = 1150$, $F_r = 0.19$, $\alpha = 83°$, and $a/R = 0.3$.

tical physical parameters: $R_e = 1150$, $F_r = 0.19$, $\alpha = 83°$, and $a/R = 0.3$. The decrease of $\omega_{y\max}$ accompanied by an increase in $\omega_{z\max}$ of comparable magnitude is a clear indication and measure of the surface connection. The overall comparison between measurement and computation is quite satisfactory.

4. Numerical results

To understand the mechanisms of vortex connection at a free surface and dependence on physical parameters, we perform six simulations with different Reynolds numbers, Froude numbers, and initial incidence angles of the vortex ring. These parameters for each simulation are listed in table 2. We organize our analysis of the numerical results as follows: § 4.1 presents general features of the vortex connection;

§4.2 details the mechanisms of vorticity transformation and the role of the surface layers in these transformations; §4.3 looks at a definition of vortex connection time based on streamline topology and examines its dependence on Reynolds and Froude numbers, and initial incidence angle.

4.1. *General features of vortex connection at a free surface*

4.1.1. *Evolution of vorticity iso-surface and vortex line structures*

The evolution of the vortex ring as it approaches and meets the free surface is shown in figure 5 where iso-surfaces of vorticity are plotted at successive times. For reference, the corresponding free-surface elevations created by the approaching/connecting vortex are also plotted. A different and often useful way to show the vorticity evolution is to plot representative vortex filaments which are shown in figure 6 at three of the time instants shown in figure 5. Note that the box shown translates with the vortex ring.

The main features and stages of the connection process are shown in the evolution of the primary (ring) and secondary (free-surface) vorticity:

(*a*) The vortex ring approaching the free surface ($t = 3$, figures 5*a*, 6*a*) is accompanied by the deformation of the free surface and the generation of secondary surface vorticity to obtain the value given by (2.16) and (2.17).

(*b*) The ring vortex impinges the surface vorticity at $t \sim 5$ (figure 5*b*, *g*). The top portion of the ring deforms and stretches near the free surface. The iso-surface of surface secondary vorticity is 'bent' by the induced flow which is reflected also in the crescent-like surface depression.

(*c*) At $t \sim 6$ (figures 5*c*, 6*b*), some of the vortex lines aft of the main tube disconnect and attach to the free surface, resulting in a pair of counter-rotating normal vortices on the free surface. Note that the connection (indicated say by the two broken/connected vortex filaments in figure 6*b*) occurs at the aft portion and towards the two 'shoulders' of the vortex ring. Figure 6*b* (and 6*a*) also indicates vortex stretching near the symmetry plane $y = 0$ both in the primary and surface vorticity resulting in stronger vorticity magnitudes near this centre-plane. On the free surface, a pair of surface depressions ('dimples') are seen. (A single positive surface elevation forward of the dimple pair due to the induced velocity of the main approaching ring is now also quite distinct.)

(*d*) At $t \sim 8$ (figure 5*d*), the surface dimples move apart indicating the widening of the underlying U-shaped vortex structure. Near the centre-plane, the unconnected (surface-parallel) vorticities are advected forward due to velocity induced by the remaining ring. The horizontal vorticity near the free surface everywhere undergoes large viscous dissipation (cf. §4.2). This effect is particular observable near the centre-plane as much of the (surface-parallel) vorticity is diminished and eventually vanishes (see figure 5*e*).

(*e*) At $t = 10$ (figure 5*e*) the break-up of the primary vortex and its connection to the surface have already past completion. The two surface dimples continue to move apart and only connected (surface-normal) vorticity remains at the free surface.

(*f*) Figures 5(*f*) and 6(*c*) at $t = 30$ show the features occurring during the second connection, this time involving the lower limb of the ring. The vortex mechanisms are similar to the first connection. The second connection leads to a second pair of surface dimples inside and forward of the first pair. The main underlying vorticity is now in the form of two U-shaped (a single W-shaped) vortices with the outer/inner limbs associated respectively with the first/second connections. These two U-vortices eventually separate and move apart on either side of the centre-plane.

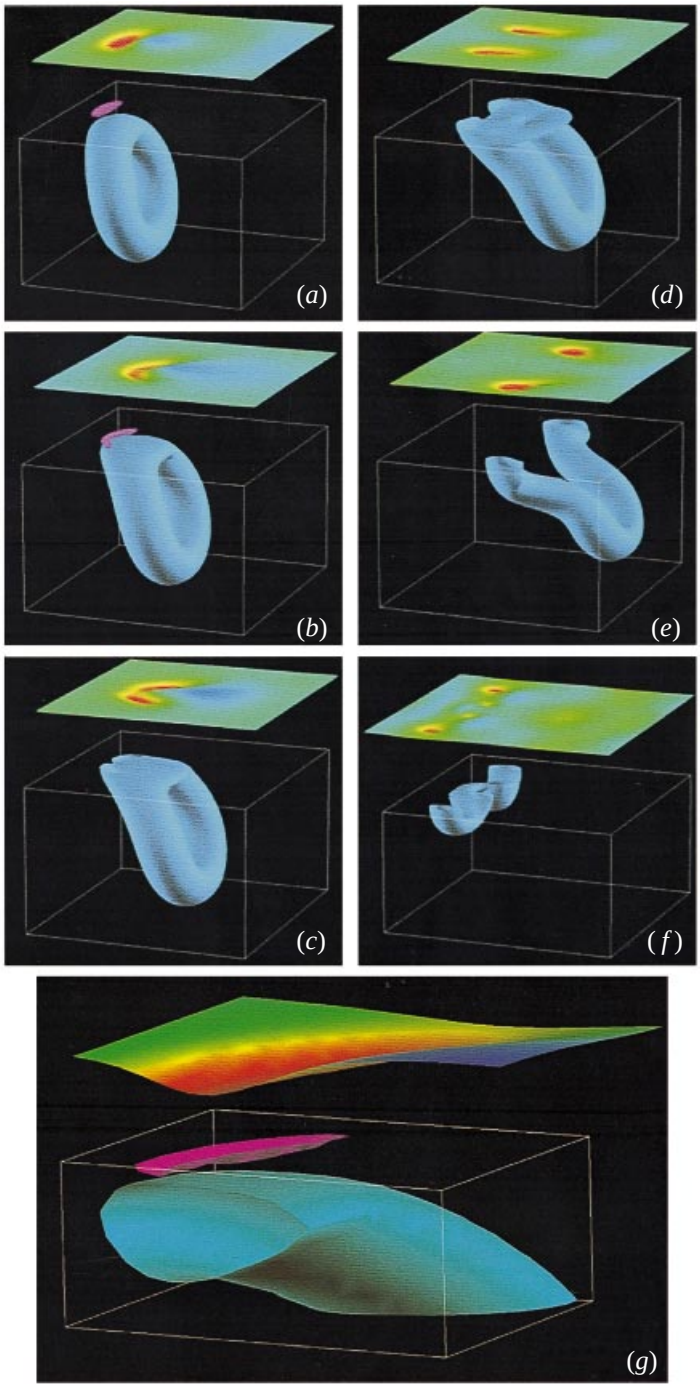

FIGURE 5. Evolution of the vortex ring and the free-surface elevation for Case II. Iso-surfaces of vorticity are plotted for: the primary vortex at 12.5% of the initial maximum value (blue); and secondary near-surface vorticity at 5% of the initial maximum value (magenta). The free-surface displacement (blue for elevation and red for depression) is plotted above (displaced vertically for clarity). The plots are shown at times: $t =$ (*a*) 3; (*b*) 5; (*c*) 6; (*d*) 8; (*e*) 10; (*f*) 30; and (*g*) close-up of (*b*) near the free surface (only one of the symmetric sides is shown).

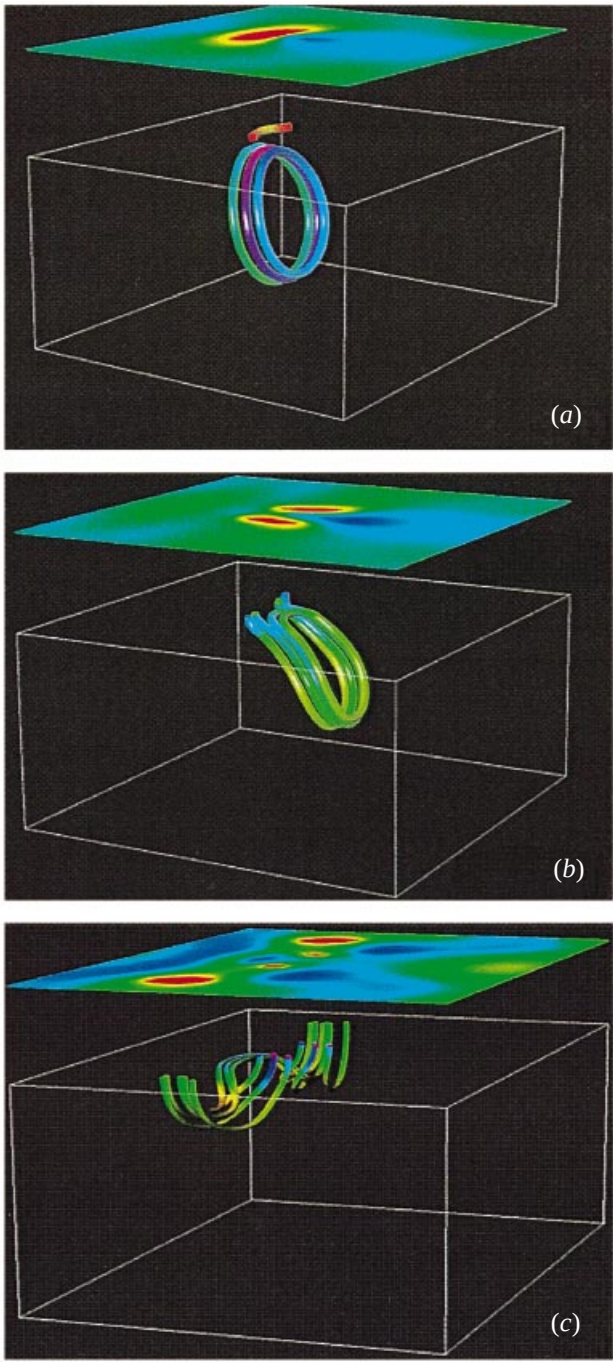

FIGURE 6. Evolution of the vortex ring and the free-surface elevation for Case II. Representative vortex filaments are shown for the primary vortex and secondary near-surface vorticity. The magnitude of the vorticity along the filaments is indicated by colours (purple/blue is greater than red). The free-surface displacement (blue for elevation and red for depression) is plotted above (displaced vertically for clarity). The plots are shown at times: $t =$ (*a*) 3; (*b*) 6; (*c*) 30.

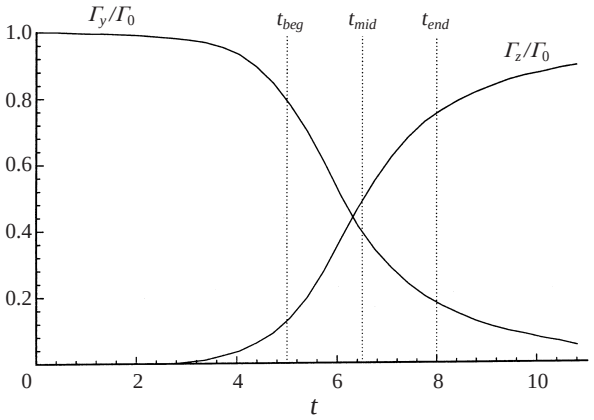

FIGURE 7. Evolution of velocity circulations for Case II: Γ_y on the centre-plane $y = 0$; and Γ_z on the free surface $z = 0$; normalized by initial ring circulation Γ_0.

Many of the above features of first and second connections to a free surface resemble what has been visualized experimentally (Bernal *et al.* 1989; Gharib *et al.* 1992; Gharib & Weigand 1996).

4.1.2. *Evolution of velocity circulation and maximum vorticity*

The main quantitative feature of vortex connection is the rapid decrease of the total enstrophy of the original vortex tube on the centre (vertical) plane accompanied by a comparable increase of enstrophy on the normal (horizontal) plane.

Figure 7 plots the evolution of the total circulations: Γ_y around the upper limb of the vortex ring on $y = 0$; and Γ_z on $z = 0$ (for $y > 0$), for Case II. The rate of decrease (increase) of Γ_y (Γ_z) is large during $5 \lesssim t \lesssim 8$. Kinematic processes resulting in the transfer of Γ_y to Γ_z are also observed in computations (but for a free-slip wall) by Melander & Hussain (1990) and Kida *et al.* (1991); and experimentally by Gharib & Weigand (1996) and Willert & Gharib (1997).

Based on figure 7 and the qualitative pictures of § 4.1.1, we can identify three (very) approximate times which separate the different phases of the connection process (for Case II): $t = t_{beg} \sim 5$ which marks the beginning of the connection (when Γ_y/Γ_z in figure 7 have decreased/increased appreciably); $t = t_{mid} \sim 6.5$ (when $\Gamma_y \sim \Gamma_z$ in figure 7) marking roughly the mid-point of the connection; and the end of the (first) connection $t = t_{end} \sim 8$ (when Γ_y, Γ_z have reached an appreciable fraction of their asymptotic values). These are useful for later reference.

An alternative to velocity circulation is to consider the maximum vorticity magnitudes on the symmetry and free-surface planes. Their evolution is plotted for Case II in figure 3(*a*). The behaviour is qualitatively similar to that in figure 7 but with $\omega_{z\max}$ displaying an appreciable post-connection decay due to viscous diffusion.

4.1.3. *Free-surface elevation*

As mentioned earlier, an important feature of the vortex connection to a free surface is the deformation of the free surface during the vortex/surface interaction and resulting generation of surface vorticity. For this problem, to leading order, the free-surface elevation η is related to the induced surface velocity in two ways: surface normal velocity w which correlates (positively) with η_t via the kinematic condition

(2.10); and surface-parallel velocity magnitude which correlates (negatively) with η via the normal-stress free-surface condition (2.13) as a Venturi effect.

In figure 3(*b*), it is seen that total surface wave energy rises before connection takes place and has indeed past its maximum value when connection begins (at t_{beg}). The surface elevation features are seen in figures 5 and 6. There are two basic patterns of surface deformation above the connecting vortex ring depending on whether it is in the early or late stages of vortex connection: (i) in the early stage of connection (t somewhat less than t_{mid}), the free surface has a crescent-shaped depression slightly behind the upper limb of the impinging vortex ring (see figure 9); and (ii) in the later stage of connection ($t \gtrsim t_{mid}$), there are surface depressions (dimples) associated with connected vortices. These two free-surface patterns are shown clearly in figure 8.

The question of whether ω_z on $z = 0$ correlates well with pressure and/or elevation at the surface is of some importance since the latter are often used to indicate the former and hence deduce the location and duration of surface connection (see e.g. Bernal & Kwon 1989; and Dommermuth 1993 who discussed this point). Figure 8 also plots the dynamic pressure p and normal vorticity ω_z on $z = 0$. Comparing the surface elevation η with p and ω_z, it is found that η and p correlate well, in general, while η and ω_z much less so. The former can be seen as a consequence of the condition of vanishing total normal stress, (2.13), where η/Fr^2 differs from p by only a viscous term $2w_z/R_e$ which is small for large R_e.

The poor correlation between η and surface ω_z turns out to be generally true. Indeed, except for axisymmetric ω_z distributions, neither the extrema nor contours of η and ω_z correlate well. Some specific examples are given in the Appendix. That surface patterns do not in general provide reliable information on connected surface vorticity has an immediate consequence for experimental observations where visualization or measurements of the former (say using shadowgraphs or wave probes) are often relied upon to understand the features of the latter. This is especially so when ω_z contours are not circular/axisymmetric as in the early connection stage.

4.1.4. *Secondary surface vorticity*

Figures 5 and 6 show the generation of induced secondary vorticity just beneath the free surface which is prominent for $t \lesssim t_{mid}$. Such surface vorticity plays an important role in free-surface vortex connection as pointed out by the measurements of Gharib *et al.* (1992) and Gharib & Weigand (1996).

The generation of surface (parallel) vorticity is directly related to the free-surface deformations (and induced surface-parallel velocities) according to (2.16) and (2.17). As the primary vortex approaches the free surface, the main surface deformation is a crescent-shaped depression near $y = 0$ (cf. figures 5*b*, 8*a*). The associated surface vorticity is thus also concentrated near the centre-plane.

We plot in figure 9 at time $t = 4$ ($< t_{beg}$) on the symmetry line $y = 0$, the longitudinal variations of $\eta(x)$, the longitudinal velocity $u(x)$, $\omega_y^s(x)$, and the surface values of $-2u\eta_{xx}$ and $-2\eta_{xt}$ (see (2.17)). Note that on this symmetry line, the terms contributing to ω_y^s in (2.17) which are associated with three-dimensional effects (Longuet-Higgins 1998) vanish. As a reference, we plot also the transverse vorticity of the primary vortex $\omega_y(x)$ on the centre-plane (at $z = -0.4$ where the core is). Comparing $\eta(x)$ to $u(x)$, we see the direct correlation of the surface depression with the induced tangential velocity. Owing to the inclination angle of the ring α ($= 80^\circ$ in this case), however, η is shifted slightly backwards relative to $\omega_y(x)$ of the upper limb of the ring. The surface secondary vorticity ω_y^s has (mainly) an opposite sign to the primary ω_y as expected. The correlation between η and ω_y^s is, however, less direct, the

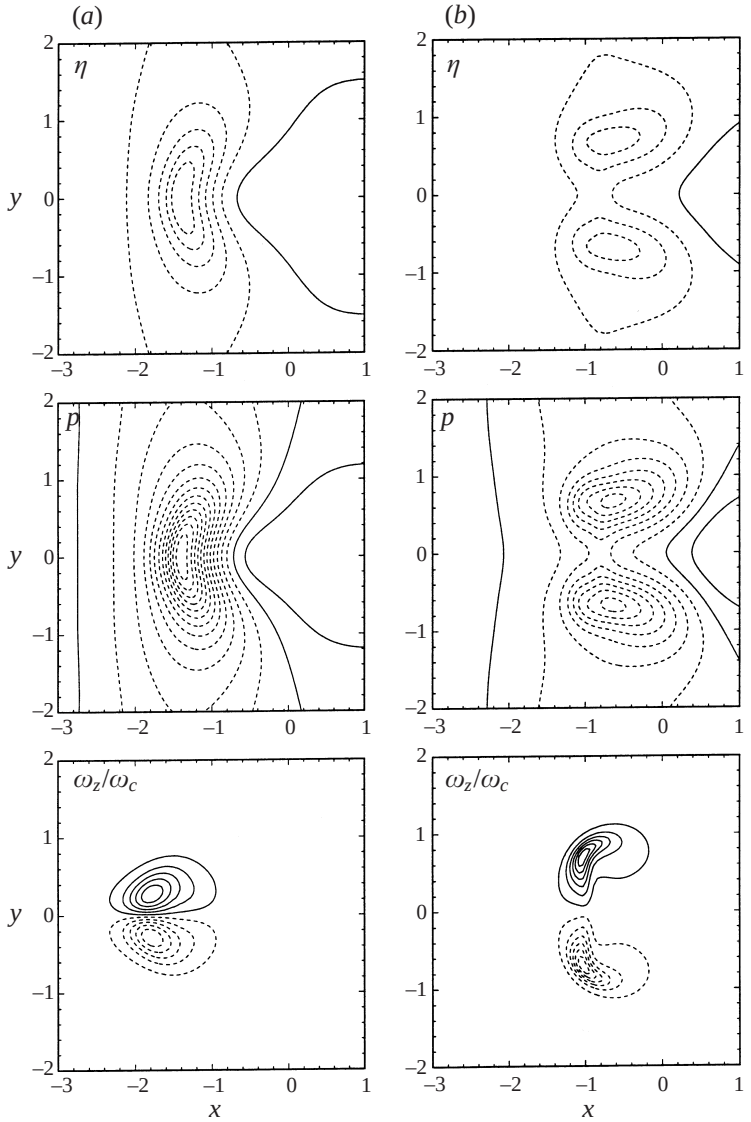

FIGURE 8. Contours of free-surface elevation η (contour increment 0.004); dynamic pressure p (contour increment 0.008); and surface-normal vorticity ω_z/ω_c (contour increments 0.02 at $t = 5.5$ and 0.1 at $t = 8$) for Case II for: (*a*) early connection stage $t = 5.5$; and (*b*) late connection stage $t = 8$. Solid/dashed lines represent positive/negative contour values.

latter being a combination of two effects: the curvature effect $-2u\eta_{xx}$ (u is negative, and η_{xx} is large/positive near the centre of the η depression and small/negative elsewhere); and the unsteady effect $-2\eta_{xt}$ of comparable magnitude and similar sign as $-2u\eta_{xx}$.

The remaining terms of (2.17) represent the three-dimensional effect (cf. Longuet-Higgins 1998) and in general results in an angle θ, say, between the surface velocity (u^s, v^s) and $\boldsymbol{\omega}^s = (\omega_x^s, \omega_y^s)$ (in the absence of this effect, $\theta \equiv 90°$). Figure 10 illustrates this with vector plots of (u^s, v^s) and $\boldsymbol{\omega}^s$ and contours of $\sin\theta$. We note that

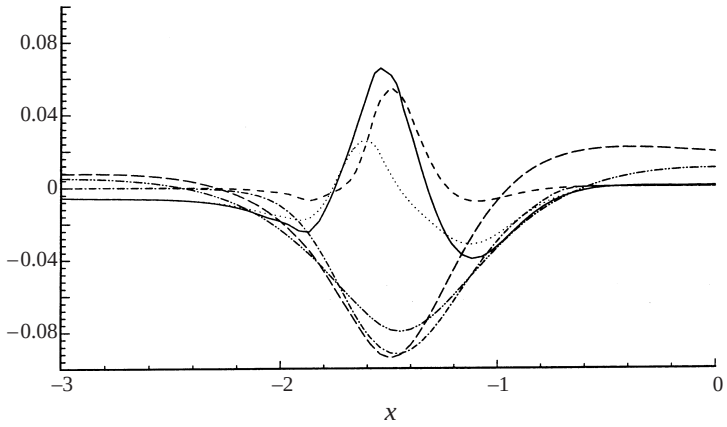

FIGURE 9. Longitudinal variations of surface ($z = 0$) quantities on the symmetry plane ($y = 0$) at $t = 4$ for Case II: —··—··— , $u/5$; — — , $\eta \times 5$; ———— , ω_y^s/ω_c; – – – – , $-2u\eta_{xx}/\omega_c$; and ····· , $-2\eta_{xt}/\omega_c$. For reference, we plot also $0.1\times\omega_y/\omega_c$ of the primary (upper limb) ring vortex on $y = 0$ and $z = -0.4$ (where the core is): – · – · – .

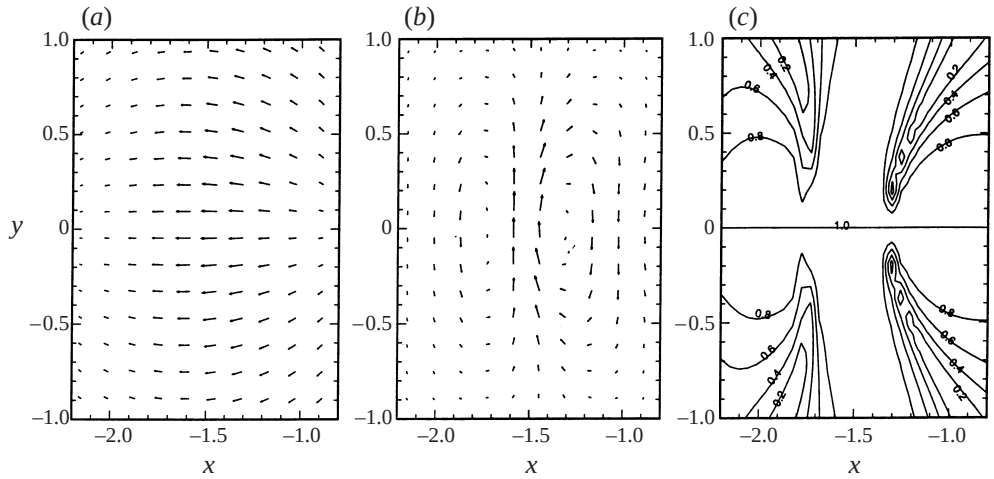

FIGURE 10. Three-dimensional effects on the surface vorticity at $t = 4$ for Case II: (*a*) surface velocity vectors (u^s, v^s); (*b*) surface vorticity vectors (ω_x^s, ω_y^s); and (*c*) contours of $\sin\theta$ where θ is the angle between (*a*) and (*b*). Note that $\sin\theta = 1$ in the absence of the three-dimensional contributions to $\boldsymbol{\omega}^s$.

$\sin\theta \approx 1$ everywhere $|\boldsymbol{\omega}^s|$ is appreciable, and the three-dimensional contributions are appreciable only away from the centreline and the axis of maximum ω_y^s.

4.1.5. *Vorticity flux at the free surface*

The vorticity flux at a free surface is a useful way to demonstrate vortex connection and the disappearance of horizontal vorticity during connection is associated with its viscous flux out of the free surface (e.g. Lugt 1987; Rood 1994*a*, *b*; Gharib & Weigand 1996).

Figure 11 plots the longitudinal variation of the transverse vorticity flux $R_e^{-1}\partial\omega_y/\partial z$ on $y = z = 0$ compared to the distribution of ω_y on the $y = 0$ plane during connection. Note that ω_y is negative here hence figure 11 indicates that (negative)

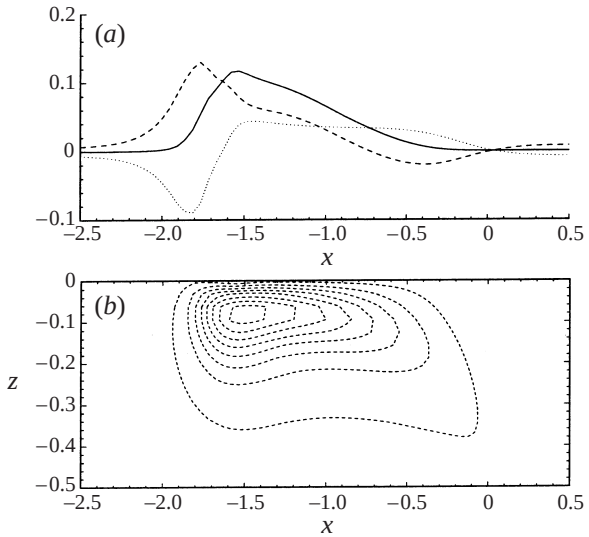

FIGURE 11. (*a*) Longitudinal variation of vorticity flux $R_e^{-1}\partial\omega_y/\partial z$ at $t = 7$ on $y = z = 0$: ———— , $R_e^{-1}\partial\omega_y/\partial z$; – – – – , $\partial u/\partial t$; · · · · · · · , $\partial(u^2/2 + p)/\partial x$. (Note that $R_e^{-1}\partial\omega_y/\partial z$ is indistinguishable from the sum of $\partial u/\partial t$ and $\partial(u^2/2 + p)/\partial x$.) (*b*) Contours of ω_y/ω_c on $y = 0$ (the contour increment is 0.05).

transverse vorticity is fluxed out of the fluid as the primary vortex impinges the surface.

From (2.1) and (2.2), the vorticity flux $R_e^{-1}\partial\omega_y/\partial z$ can be written as

$$\begin{aligned}\frac{1}{Re}\frac{\partial\omega_y}{\partial z} &= \frac{1}{Re}\frac{\partial}{\partial z}\left(\frac{\partial u}{\partial z} - \frac{\partial w}{\partial x}\right)\\ &= \frac{1}{Re}\left(\frac{\partial^2 u}{\partial z^2} + \frac{\partial^2 u}{\partial x^2} + \frac{\partial^2 v}{\partial x\partial y}\right)\\ &= \frac{\partial u}{\partial t} + u\frac{\partial u}{\partial x} + v\frac{\partial u}{\partial y} + w\frac{\partial u}{\partial z} + \frac{\partial p}{\partial x} + \frac{1}{Re}\left(\frac{\partial^2 u}{\partial y^2} + \frac{\partial^2 v}{\partial x\partial y}\right).\end{aligned} \tag{4.1}$$

On the symmetry plane $y = 0$, $v\,\partial u/\partial y$ and $R_e^{-1}\partial^2 v/\partial x\partial y$ vanish, $R_e^{-1}\partial^2 u/\partial y^2$ is negligible, and (4.1) can be approximated by its two-dimensional form. Near the free surface, the term $w\partial u/\partial z$ is negligible, and we finally obtain

$$\frac{1}{Re}\frac{\partial\omega_y}{\partial z} \approx \frac{\partial u}{\partial t} + \frac{\partial}{\partial x}\left(\frac{u^2}{2} + p\right) \tag{4.2}$$

for $y, z \approx 0$. Thus, the vorticity flux on the symmetry plane near the free surface contains two contributions: acceleration of the tangential velocity u and the tangential gradient of the energy head $u^2/2 + p$. In the latter term, the deviation of p on $z = 0$ from its constant value at $z = \eta$ cannot in general be neglected. The two separate contributions in (4.2) are also plotted in figure 11(*a*). The magnitudes of the two contributions are comparable at this phase of the connection process.

It is useful to define the total viscous flux of the vorticity at the surface as

$$\mathscr{F}_i \equiv \frac{1}{R_e}\int\!\!\int \left.\frac{\partial\omega_i}{\partial z}\right|_{z=0} \mathrm{d}x\mathrm{d}y \equiv \frac{1}{R_e}\left\langle \left.\frac{\partial\omega_i}{\partial z}\right|_{z=0}\right\rangle, \quad i = x, y, z, \tag{4.3}$$

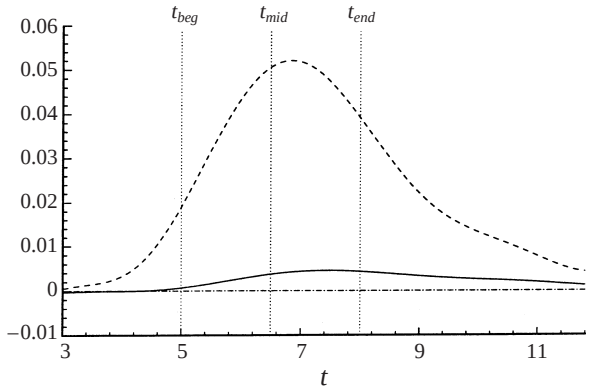

FIGURE 12. Time evolution of the vorticity flux at the free surface: ———— , $\mathscr{F}_x$; – – – – , $\mathscr{F}_y$; – · – · – , $\mathscr{F}_z$.

where here and hereafter, the integration implied by $\langle \cdot \rangle$ is performed over the $y \geqslant 0$ half-plane only, since the flow is symmetric. Figure 12 plots the time evolution of $\mathscr{F}_x$, $\mathscr{F}_y$, and $\mathscr{F}_z$. While $\mathscr{F}_z$ is negligible, the viscous flux of horizontal vorticity is significant during connection especially $\mathscr{F}_y$ which reaches a maximum value just after t_{mid}. (Note that positive values of $\mathscr{F}_y$ imply outward flux of negative primary transverse vorticity.) The results agree well with previous studies.

The different behaviours of the components of $\mathscr{F}$ can be understood from the dynamic free-surface boundary conditions and the concept of a free-surface viscous layer (see § 4.2.1). As we show later, ω_x, ω_y, and $\partial\omega_z/\partial z$ (but not ω_z itself) diminish rapidly over a thin viscous surface layer, so that at the free surface, $\partial\omega_x/\partial z$, $\partial\omega_y/\partial z$ are large while $\partial\omega_z/\partial z$ is negligible. As a result, the outward viscous fluxes of ω_x, ω_y are large and are responsible for the disappearance of ω_x, ω_y in the viscous layer. For ω_z, $\mathscr{F}_z$ is small and the surface-normal vorticity increases during the connection. Thus, outward flux of horizontal vorticity is the key mechanism for vortex disconnection at a free surface.

4.2. *Detailed mechanism of vortex connection at a free surface*

A main objective of this study is to obtain, using numerical simulations, the detailed structures and mechanisms of vortex connection at a free surface. For specificity, we consider case II of table 2.

We find that a key to this understanding is to identify the surface layers – an outer blockage layer associated with the free-surface kinematic boundary condition, and an inner viscous layer due to the stress-free dynamic condition at the free surface – and the different mechanisms of vortex evolution/transformation in each layer.

4.2.1. *Surface viscous and blockage layers*

A free surface affects the underlying flow by means of two mechanisms: first, the dynamic boundary conditions require that the tangential stresses at the surface vanish; second, the kinematic boundary condition constrains the motion normal to the surface. These two mechanisms respectively cause two distinct regions near the free surface: an inner *viscous layer* and an outer *blockage layer*.

The blockage layer is the region where the kinematic boundary condition is felt. Throughout the blockage layer, the vertical velocity component diminishes. From

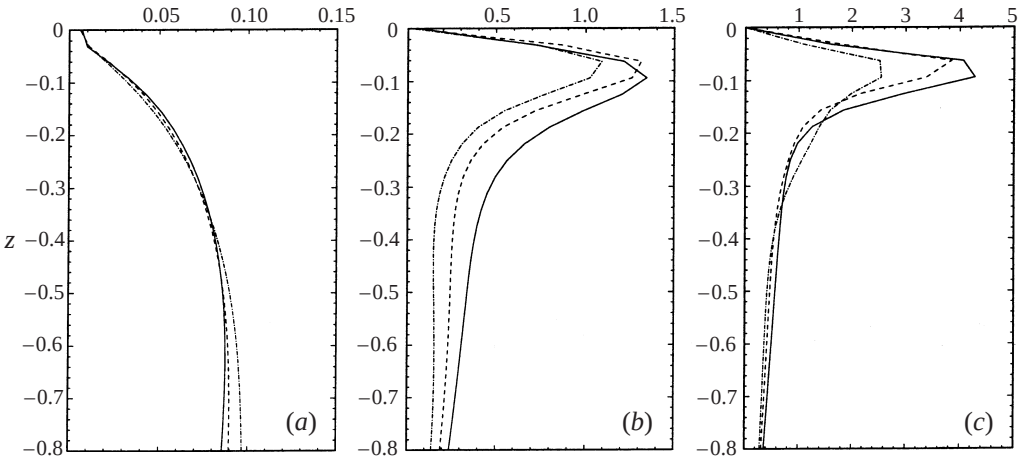

FIGURE 13. Vertical variations in the surface layers for Case II. (*a*) $\langle w^2 \rangle$; (*b*) $\langle \omega_y^2 \rangle$; and (*c*) $\langle (\partial \omega_z / \partial z)^2 \rangle$ at $t =$: ———— , 6; – – – – , 7; – · – · – , 8.

continuity (2.2), the thickness of the blockage layer δ^b should be comparable to the characteristic length scale of the flow.

The surface viscous layer is due to the vanishing of the tangential stresses at the surface. It is therefore a result of viscous effects and is absent, for example, in Euler flow. In contrast to the blockage layer, the viscous layer near the surface does not affect the velocity but instead the vertical variations of the horizontal vorticity components ω_x, ω_y, and the z-derivative of the vertical vorticity component, $\partial \omega_z / \partial z$. From (2.12), (2.11) we have

$$\left.\begin{aligned} \omega_x &= \frac{\partial w}{\partial y} - \frac{\partial v}{\partial z} = O(\varepsilon) \\ \omega_y &= \frac{\partial u}{\partial z} - \frac{\partial w}{\partial x} = O(\varepsilon) \end{aligned}\right\} \quad \text{on} \quad z = 0. \tag{4.4}$$

Using the fact that vorticity is divergence free, we obtain

$$\frac{\partial \omega_z}{\partial z} = -\frac{\partial \omega_x}{\partial x} - \frac{\partial \omega_y}{\partial y} = O(\varepsilon) \quad \text{on} \quad z = 0. \tag{4.5}$$

Therefore, at small Froude numbers, the values of ω_x, ω_y, and $\partial \omega_z / \partial z$ (but not ω_z itself) change from their 'outer' values to small surface values over the distance of the viscous layer. In a way similar to Prandtl's boundary layer near a solid wall, the balance between viscous and convection terms in the evolution equations for ω_x or ω_y gives the thickness of this viscous layer, $\delta^v \sim Re^{-1/2}$.

The presence of the two surface layers in the vortex connection process is shown in figures 13 at different t. Figure 13(*a*) plots the variations of $\langle w^2 \rangle$ with z which reveal a blockage layer for $z \gtrsim -0.4$. As mentioned above, the viscous layer manifests as the sharp decrease of ω_x, ω_y, $\partial \omega_z / \partial z$. Figures 13(*b*), 13(*c*) plot $\langle \omega_y^2 \rangle$ and $\langle (\partial \omega_z / \partial z)^2 \rangle$ which show clearly a viscous layer of thickness $\delta^v \sim 0.1$.

The importance of the blockage layer is that the bulk of vortex stretching and turning occur in this layer as the vortex approaches the surface, reaching their maximum rates at the lower boundary of the viscous layer. Viscous effects take over in the inner viscous layer and are responsible for the disappearance of transverse

vorticity and the strengthening of surface normal vorticity. These are elucidated below.

4.2.2. *Vorticity transformations in the surface layers*

The equation for vorticity evolution is

$$\frac{\mathrm{D}\boldsymbol{\omega}}{\mathrm{D}t} = \boldsymbol{\omega}\cdot\nabla\boldsymbol{V} + \frac{1}{Re}\nabla^2\boldsymbol{\omega}. \tag{4.6}$$

The first term on the right hand side of (4.6) is associated with the vortex stretching and turning, and can be rewritten as

$$\nabla\boldsymbol{V} = \tfrac{1}{2}(\nabla\boldsymbol{V} + (\nabla\boldsymbol{V})^T) + \tfrac{1}{2}(\nabla\boldsymbol{V} - (\nabla\boldsymbol{V})^T) = \boldsymbol{S} + \tfrac{1}{2}\boldsymbol{D},$$

where $\boldsymbol{S}$ and $\boldsymbol{D}$ are respectively the symmetric and antisymmetric strain rate tensors:

$$[S_{ij}] \equiv \frac{1}{2}\left(\frac{\partial u_i}{\partial x_j} + \frac{\partial u_j}{\partial x_i}\right),$$

$$\boldsymbol{D} \equiv \begin{bmatrix} 0 & -\omega_3 & \omega_2 \\ \omega_3 & 0 & -\omega_1 \\ -\omega_2 & \omega_1 & 0 \end{bmatrix}.$$

For any vector $\boldsymbol{A}$, we have $\boldsymbol{A}\cdot\boldsymbol{D} = \boldsymbol{A}\times\boldsymbol{\omega}$. Therefore,

$$\boldsymbol{\omega}\cdot\nabla\boldsymbol{V} = \boldsymbol{\omega}\cdot(\boldsymbol{S} + \boldsymbol{D}/2) = \boldsymbol{\omega}\cdot\boldsymbol{S} + \boldsymbol{\omega}\times\boldsymbol{\omega}/2 = \boldsymbol{\omega}\cdot\boldsymbol{S}.$$

Thus, (4.6) can be written as

$$\frac{\mathrm{D}\boldsymbol{\omega}}{\mathrm{D}t} = \boldsymbol{\omega}\cdot\boldsymbol{S} + \frac{1}{Re}\nabla^2\boldsymbol{\omega}. \tag{4.7}$$

The physical meaning of $\boldsymbol{\omega}\cdot\boldsymbol{S}$ is clarified if we decompose it into two perpendicular directions (see figure 14): one along $\boldsymbol{\omega}$, which we denote by the unit vector $\boldsymbol{e}_\omega$, and the other in the $(\boldsymbol{\omega}\cdot\boldsymbol{S})$-$\boldsymbol{\omega}$ plane, which we denote by the unit vector $\boldsymbol{e}_t$. That is, $\boldsymbol{e}_\omega \equiv \boldsymbol{\omega}/|\boldsymbol{\omega}|$, and, $\boldsymbol{e}_t \equiv (\boldsymbol{\omega}\cdot\boldsymbol{S} - (\boldsymbol{\omega}\cdot\boldsymbol{S}\cdot\boldsymbol{e}_\omega)\boldsymbol{e}_\omega)/|\boldsymbol{\omega}\cdot\boldsymbol{S} - (\boldsymbol{\omega}\cdot\boldsymbol{S}\cdot\boldsymbol{e}_\omega)\boldsymbol{e}_\omega|$. With these definitions, (4.7) can be written as

$$\frac{\mathrm{D}\boldsymbol{\omega}}{\mathrm{D}t} = (\boldsymbol{\omega}\cdot\boldsymbol{S}\cdot\boldsymbol{e}_\omega)\boldsymbol{e}_\omega + (\boldsymbol{\omega}\cdot\boldsymbol{S}\cdot\boldsymbol{e}_t)\boldsymbol{e}_t + \frac{1}{Re}\nabla^2\boldsymbol{\omega} \equiv \mathscr{V}_s\boldsymbol{e}_\omega + \mathscr{V}_t\boldsymbol{e}_t + \mathscr{V}_d, \tag{4.8}$$

where the vortex stretching term is $\mathscr{V}_s \equiv \boldsymbol{\omega}\cdot\boldsymbol{S}\cdot\boldsymbol{e}_\omega$, the turning term $\mathscr{V}_t \equiv \boldsymbol{\omega}\cdot\boldsymbol{S}\cdot\boldsymbol{e}_t$, and the diffusion term $\mathscr{V}_d \equiv Re^{-1}\nabla^2\boldsymbol{\omega}$.

The main consequence of vorticity connection at the free surface is the increase in the normal component ω_z accompanied by decrease in the horizontal vorticity component (in this case ω_y). For later reference, we write the components of (4.8) as

$$\frac{\mathrm{D}\omega_i}{\mathrm{D}t} = \mathscr{V}_{si} + \mathscr{V}_{ti} + \mathscr{V}_{di}, \quad i = x, y, z, \tag{4.9}$$

where $\mathscr{V}_{si} \equiv \mathscr{V}_s(\boldsymbol{e}_\omega\cdot\boldsymbol{e}_i)$, $\mathscr{V}_{ti} \equiv \mathscr{V}_t(\boldsymbol{e}_t\cdot\boldsymbol{e}_i)$, and $\mathscr{V}_{di} \equiv R_e^{-1}\nabla^2\omega_i$ $(i = x, y, z)$ are respectively the stretching, turning and diffusion components in the ith direction. Note that $\mathscr{V}_d$ is the gradient of the vorticity flux discussed in § 4.1.5.

We first investigate averaged quantities over a horizontal (half) plane. Figure 15 plots the vertical variation of $\langle\mathscr{V}_s\rangle$ and $\langle\mathscr{V}_t\rangle$ at $t = 7$. As the primary vortex approaches the free surface, both stretching $\langle\mathscr{V}_s\rangle$ and turning $\langle\mathscr{V}_t\rangle$ increase over the blockage layer and then decrease rapidly within the viscous layer. According to (4.4), at the free surface, $\omega_x, \omega_y \sim O(\varepsilon) \ll \omega_z$, vorticity is almost perpendicular to the free

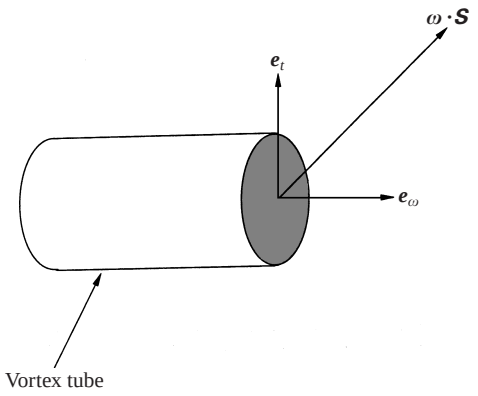

FIGURE 14. Definition sketch of $\boldsymbol{\omega} \cdot \boldsymbol{S}$, $\boldsymbol{e}_\omega$ and $\boldsymbol{e}_t$.

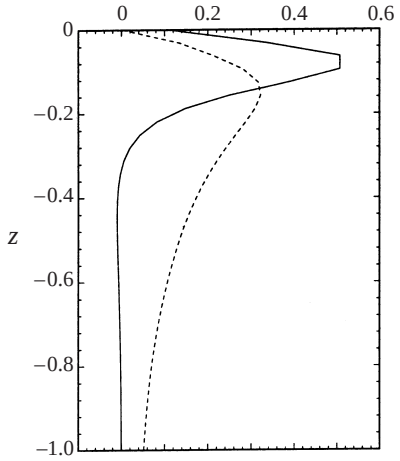

FIGURE 15. Vertical variation of $\langle \mathscr{V}_s \rangle$ (————), and $\langle \mathscr{V}_t \rangle$ (– – – –) for Case II at $t = 7$.

surface and therefore there is little vortex turning taking place at the surface. Vortex stretching, dominated by $\mathscr{V}_{sy}$ in the blockage layer, also decreases over the viscous layer because ω_y itself diminishes. Unlike $\langle \mathscr{V}_t \rangle$, $\langle \mathscr{V}_s \rangle$ still has a finite value at the free surface because of the stretching of ω_z (as pointed out earlier, it is ω_x, ω_y, $\partial\omega_z/\partial z$, but not ω_z, that decrease over the surface layer).

Figure 16 plots the components of vortex stretching, turning and diffusion: $\langle \mathscr{V}_{\ell i} \rangle$, $\ell = s, t, d$ and $i = x, y, z$. Note that, since $\langle \omega_y \rangle$ (associated with the ring) is negative as is $\langle \omega_x \rangle$ (for $y > 0$ half plane for $0^\circ < \alpha < 90^\circ$), positive values of $\langle \mathscr{V}_{\ell i} \rangle$ for $i = x, y$ decrease the magnitude of that vorticity component; while the opposite is true for $\langle \mathscr{V}_{\ell z} \rangle$ (since $\langle \omega_z \rangle$ is positive for the $y > 0$ half plane). From these plots, we observe the following. (i) All components of stretching increase inside the blockage layer. Over the viscous layer, stretching of ω_x and ω_y drops sharply while stretching of ω_z does not diminish. (ii) The magnitudes of all turning terms increase over the blockage layer and reach their maxima around the lower boundary of the viscous layer ($z \sim -\delta^v$). For $z > -\delta^v$, these magnitudes decrease – ω_y loses through vortex turning while ω_z gains. (iii) Diffusion becomes significant near the surface. This leads to a decrease of

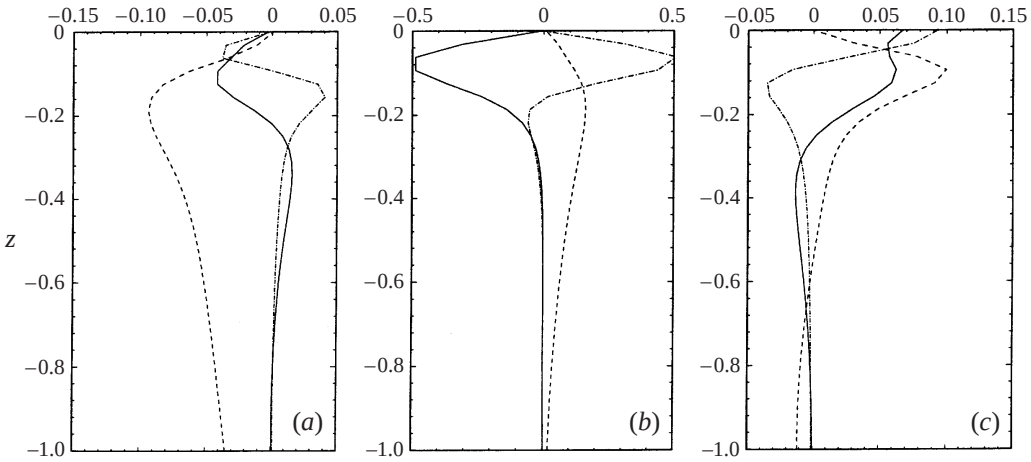

FIGURE 16. Vertical variations of the components of vortex stretching, turning and diffusion, $\langle \mathscr{V}_{\ell i} \rangle$ at $t = 7$ for $i = (a)\ x$; $(b)\ y$ and $(c)\ z$. The lines are: ———— , stretching ($\ell = s$); – – – – , turning ($\ell = t$); and – · – · – , diffusion ($\ell = d$). Note that the magnitude scales are different in each figure.

$|\langle \omega_y \rangle|$ which is fluxed out of the free surface (§ 4.1.5), and a transport of $\langle \omega_z \rangle$ towards the surface where it increases ($\mathscr{F}_z$ is negligible at the surface, cf. figure 12).

The time evolution of $\langle \mathscr{V}_{\ell i} \rangle$ also provides important information about the vortex dynamics during connection. It is convenient to study $\langle \mathscr{V}_{\ell i} \rangle(t)$ at fixed values of depth z, in which case it is important to consider also the averaged (vertical) convection, $\langle \mathscr{V}_{ci} \rangle \equiv \langle -\partial(w\omega_i)/\partial z \rangle$.

Figure 17 shows the time evolution of $\langle \omega_z \rangle$ at the free surface $z = 0$. The rate of change of $\langle \omega_z \rangle$ is equal to the sum of $\langle \mathscr{V}_{\ell z} \rangle$, $\ell = s, t, d, c$. These components are plotted separately in figure 17. As connection occurs, $\langle \omega_z \rangle$ at the surface increases due to viscous diffusion and vortex stretching, with $\langle \mathscr{V}_{dz} \rangle$ reaching a maximum at $t \sim t_{mid}$ and $\langle \mathscr{V}_{sz} \rangle$ somewhat later. Consistent with figures 15 and 16, the effect of vortex turning, $\mathscr{V}_{tz}$, is negligible at $z = 0$ for all t. Note that

$$-\langle \mathscr{V}_{cz} \rangle = \left\langle \frac{\partial w\omega_z}{\partial z} \right\rangle = \left\langle w \frac{\partial \omega_z}{\partial z} \right\rangle + \left\langle \omega_z \frac{\partial w}{\partial z} \right\rangle. \tag{4.10}$$

At the free surface, the first term of (4.10) is small since both w and $\partial\omega_z/\partial z$ are small, while the second term is approximately $\langle \mathscr{V}_{sz} \rangle$ since $\boldsymbol{\omega}$ is dominated by its normal component. Thus, the effects of $\langle \mathscr{V}_{sz} \rangle$ and $\langle \mathscr{V}_{cz} \rangle$ approximately cancel at $z = 0$ as can be seen from figure 17. Since $\langle \mathscr{V}_{sz} \rangle$, $\langle \mathscr{V}_{cz} \rangle$ approximately cancel and $\langle \mathscr{V}_{tz} \rangle$ is small, the increase of $\langle \omega_z \rangle$ in time and hence the connection itself are mainly the effect of viscous diffusion $\langle \mathscr{V}_{dz} \rangle$. This is to be expected and is consistent with the limit of $F_r \to 0$.

The picture is qualitatively different a small distance below the surface outside the viscous layer. Figure 18 shows the same quantities as figure 17 but at $z = -0.1$. In this case, $\langle \mathscr{V}_{sz} \rangle$ and $\langle \mathscr{V}_{cz} \rangle$ no longer cancel; the net contribution is positive (which increases $\langle \omega_z \rangle$) at the early connection stage ($t \lesssim t_{mid}$), but is negative (due to a larger convection) later. The role of viscous diffusion is also more complex than in figure 17: $\langle \mathscr{V}_{dz} \rangle$ increases ω_z at the very beginning of connection ($t \lesssim t_{beg}$) only, but then changes sign (after $t \sim 5.5$), so that diffusion removes ω_z at $z \lesssim -\delta^v$ (and adds it to that at $z \gtrsim -\delta^v$; cf. figure 16*c*). Vortex turning now plays an appreciable role, mainly to add to ω_z (from ω_y). In summary, at the lower boundary of the viscous surface

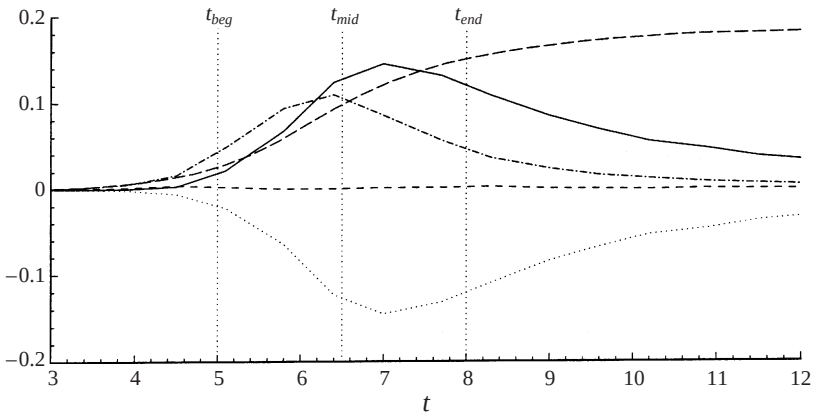

FIGURE 17. Time evolution at the free surface $z = 0$ of $\langle\omega_z\rangle/5$ (—— ——); and components of the vortex evolution $\langle\mathscr{V}_{\ell z}\rangle$, $\ell = s,t,d,c$: ———— , stretching ($\ell = s$); – – – – , turning ($\ell = t$); – · – · – , diffusion ($\ell = d$); · · · · · · · , convection ($\ell = c$).

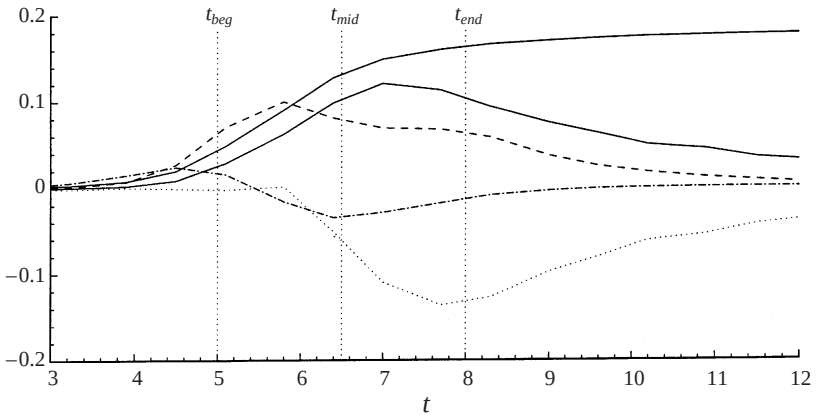

FIGURE 18. Time evolution just outside the viscous surface layer, at $z = -0.1$, of $\langle\omega_z\rangle/5$ (—— ——); and components of the vortex evolution $\langle\mathscr{V}_{\ell z}\rangle$, $\ell = s,t,d,c$: ———— , stretching ($\ell = s$); – – – – , turning ($\ell = t$); – · – · – , diffusion ($\ell = d$); · · · · · · · , convection ($\ell = c$).

layer, vortex stretching and turning are the two main processes leading to the increase of ω_z.

As seen in figure 18, outside the viscous layer, vorticity turning makes a significant contribution to ω_z. That this comes from ω_y is shown in figure 19 where we plot, at $z = -0.1$, the time evolution of $\langle\omega_y\rangle$ and $\langle\mathscr{V}_{\ell y}\rangle$, $\ell = s,t,d,c$. As the primary vortex approaches the free surface, $|\langle\omega_y\rangle|$ at this depth increases for $t < t_{mid}$ due to vortex convection $\langle\mathscr{V}_{cy}\rangle$ and stretching $\langle\mathscr{V}_{sy}\rangle$. For $t > t_{mid}$, $|\langle\omega_y\rangle|$ decreases as diffusion $\langle\mathscr{V}_{dy}\rangle$ and turning $\langle\mathscr{V}_{ty}\rangle$ overcome $\langle\mathscr{V}_{cy}\rangle$ and $\langle\mathscr{V}_{sy}\rangle$. Unlike $\langle\omega_z\rangle$, all the $\langle\omega_y\rangle$ is eventually removed by $\langle\mathscr{V}_{dy}\rangle$ and $\langle\mathscr{V}_{ty}\rangle$ after a long time.

We note that the physical problem is neither stationary nor homogeneous, and that the preceding discussions in terms of spatial averages (in the horizontal half-plane) provide in some sense only a global picture. These results can be augmented by considering spatial variations of the vorticity transformation terms which also provide information on the location and region of vortex connection.

Figure 20 plots on $z = 0$ and at $t = 7$ the contours of ω_z as well as terms

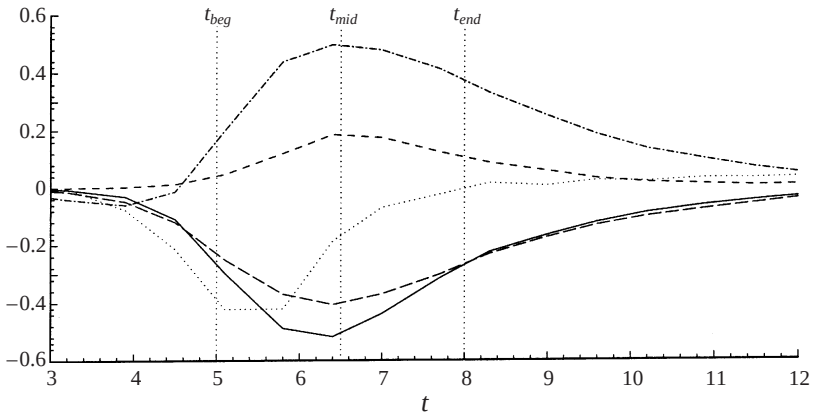

FIGURE 19. Time evolution just outside the viscous surface layer, at $z = -0.1$, of $\langle\omega_y\rangle/5$ (—— ——); and components of the vortex evolution $\langle\mathscr{V}_{\ell y}\rangle$, $\ell = s,t,d,c$: ———— , stretching ($\ell = s$); – – – – , turning ($\ell = t$); – · – · – , diffusion ($\ell = d$); · · · · · · · , convection ($\ell = c$).

contributing to its evolution. Plotted also is the contour $\mathscr{C}$ of $|\omega| = 0.25\omega_c$ at $z = -0.1$ which gives an indication of the position of the impinging primary vortex. Comparing the figures, we see that the regions of large $|\omega_z|$ correlate well with those of vortex diffusion ($\mathscr{V}_{dz}$) and stretching ($\mathscr{V}_{sz}$). Comparing to the contour $\mathscr{C}$, we note that these regions occur at the aft-shoulder areas of the primary vortex. This is consistent with the concept of 'bridging' (Kida *et al.* 1991).

The features of $\mathscr{V}_{sz}$ can be understood from the variation of $\partial w/\partial z$ induced by the primary vortex underneath. Figure 20(*d*) shows that $\partial w/\partial z$ is positive (down-wash or stretching) behind and negative (up-wash or compressing) in front of the primary vortex, with the two maxima of the former located approximately where those of $|\omega_z|$ (and $\mathscr{V}_{sz}$) are.

The contours of vorticity transformation for ω_z at $z = -0.1$ are plotted in figure 21. Different from that at the free surface, diffusion removes ω_z at the aft-shoulder regions (and puts it at the free surface, see figures 16*c* and 20*b*). Vortex stretching still helps increase ω_z, as shown in figure 20(*c*). It should be noted that at $z = -0.1$, vortex turning is another cause for the increase of ω_z at the aft-shoulder regions, which is shown clearly in figure 20(*d*).

Figure 22 plots the contours of vorticity transformation for ω_y at $z = -0.1$. The magnitudes of $\mathscr{V}_{dy}$ and $\mathscr{V}_{sy}$ are significant over the entire region bounded by $\mathscr{C}$ while $\mathscr{V}_{ty}$ is still localized at the aft-shoulder regions. Note that in this case, $\mathscr{V}_{dy}$ and $\mathscr{V}_{ty}$ contribute to the decrease of ω_y magnitude which is greater than the stretching $\mathscr{V}_{sy}$ effect which increases it.

It is useful to examine the spatial correlation of the different quantities in figures 20–22 to the rate of change of the connected (normal) vorticity on the free surface $\mathrm{D}\omega_z/\mathrm{D}t(x,y;z=0)$. Our interest is to pinpoint their specific contributions to the increase of the latter. For this purpose, we define the correlation coefficients:

$$\mathrm{Cor}\,[\mathscr{V}_{\ell i}(x,y;z=\mathrm{const})] \equiv \frac{\langle \mathrm{D}\omega_z/\mathrm{D}t(x,y;z=0)\mathscr{V}_{\ell i}(x,y;z=\mathrm{const})\rangle}{\langle(\mathrm{D}\omega_z/\mathrm{D}t(x,y;z=0))^2\rangle^{1/2}\langle(\mathscr{V}_{\ell i}(x,y;z=\mathrm{const}))^2\rangle^{1/2}}.$$

Figure 23 plots the time evolution of these correlations. For vorticity transformation quantities on the free surface $z = 0$, both $\mathrm{Cor}\,[\mathscr{V}_{sk}(z=0)]$ and $\mathrm{Cor}\,[\mathscr{V}_{dz}(z=0)]$ are positive throughout. For stretching, the correlation is high for all $t \gtrsim t_{beg}$; while

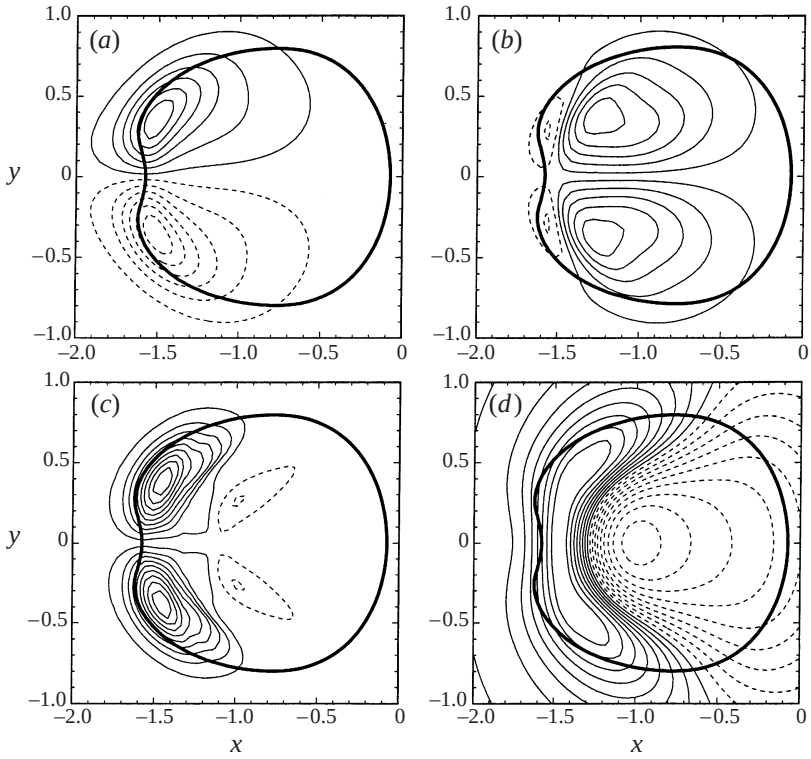

FIGURE 20. Contours on $z = 0$ at $t = 7$ of (*a*) ω_z/ω_c (contour increment 0.05); (*b*) $\mathscr{V}_{dz}$ (contour increment 0.05); (*c*) $\mathscr{V}_{sz}$ (contour increment 0.05); and (*d*) $\partial w/\partial z$ (contour increment 0.1). Solid contours represent positive values while dashed lines represent negative values. The thick line is the contour $\mathscr{C}$ corresponding to $|\omega|/\omega_c = 0.25$ at $z = -0.1$.

for diffusion, $\mathrm{Cor}\,[\mathscr{V}_{dz}(z = 0)]$ is high for $t \lesssim t_{mid}$. This behaviour agrees with the proceeding observation that the increase of surface-normal vorticity is mainly due to vortex stretching and viscous diffusion at the surface; the former is important for later times and the latter for earlier times.

As we have seen, vorticity transformations outside the surface viscous layers are important mechanisms in the surface connection. As expected, the correlation of $\mathrm{D}\omega_z/\mathrm{D}t(z = 0)$ with $\mathscr{V}_{ty}(z = -0.1)$ is high throughout the connection process indicating the main origin (the primary transverse vorticity ω_y) and mechanism (vortex turning) of the surface-connected normal vorticity. Just like at $z = 0$, vortex stretching also plays an important role here and $\mathrm{Cor}\,[\mathscr{V}_{sz}(z = -0.1)]$ is high on the average. The key vehicle of vertical vorticity transport to the free surface is viscous diffusion: $\mathrm{Cor}\,[\mathscr{V}_{dz}(z = -0.1)]$ is negative for $t_{beg} < t < t_{end}$, indicating that the removal of ω_z at this level by viscous diffusion is directly correlated with the increase of ω_z at the surface.

In conclusion, we find that the surface layers are key to understanding the mechanism of vortex connection at a free surface: In the blockage layer, ω_z increases due to vortex stretching and vortex turning (from ω_y). This vertical vorticity is then transported to the free surface through viscous diffusion over the viscous layer. This viscous diffusion and (vertical) vortex stretching at the surface are the main reasons for the increase of surface-connected normal vorticity. Two factors contribute to the

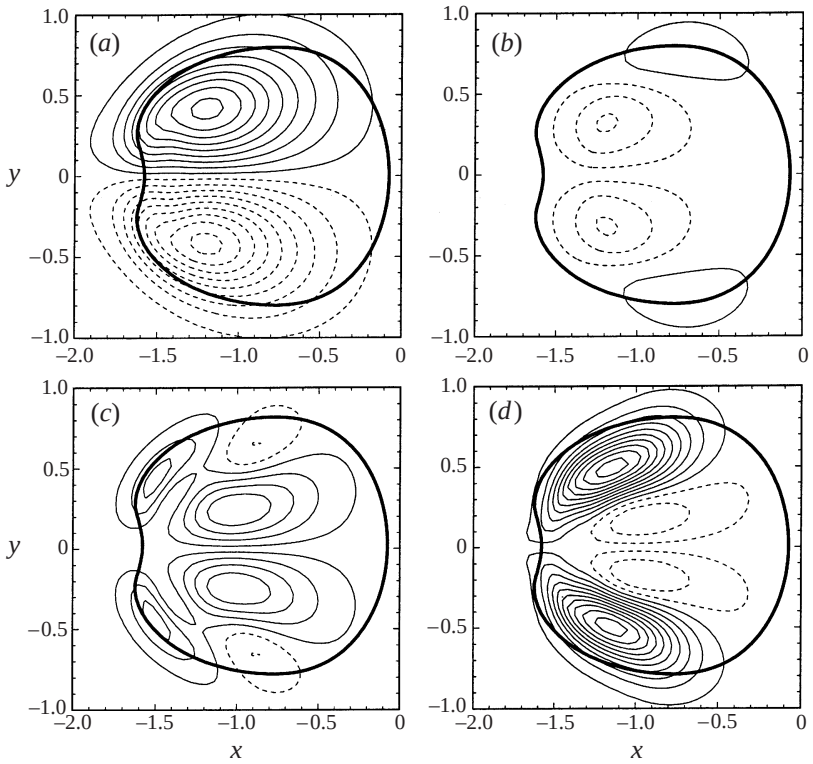

FIGURE 21. Contours on $z = -0.1$ at $t = 7$ of (*a*) ω_z/ω_c (contour increment 0.05); (*b*) $\mathscr{V}_{dz}$ (contour increment 0.05); (*c*) $\mathscr{V}_{sz}$ (contour increment 0.05); and (*d*) $\mathscr{V}_{tz}$ (contour increment 0.05). Solid contours represent positive values while dashed lines represent negative values. The thick line is the contour $\mathscr{C}$ corresponding to $|\omega|/\omega_c = 0.25$ at $z = -0.1$.

disappearance of transverse vorticity ω_y as it approaches the free surface: vortex turning of ω_y into ω_z in the blockage layer, and large diffusion of ω_y within the viscous layer (which is then fluxed out of the free surface). Figure 24 summarizes this picture schematically.

4.3. *Vortex connection time and streamline topology*

The vortex connection time or duration, T, is an important measure of the vortex connection phenomenon. The dependence of T on physical parameters of the free-surface vortex interaction (Reynolds and Froude numbers and incidence angle) is also of practical interest. A definition of T based on the discussions of § 4.1 and § 4.2 (t_{beg} and t_{end}, or appreciable changes of horizontal and vertical plane circulations) is necessarily qualitative and to some extent subjective. We propose to use a more quantitative/objective definition of T based on the topology of the streamlines on the free surface.

4.3.1. *Streamlines on the free surface and vertical symmetry plane*

Since streamlines are in general not Galilean invariant, here and hereafter we only consider them in a fixed frame (with respect to the quiescent far field). The topology of the streamlines can be classified in terms of its nodes, N, and saddle points, S. The numbers of these on a surface, say $\mathscr{N}_N$ and $\mathscr{N}_S$ respectively, satisfy specific summation rules (e.g. Hunt *et al.* 1978): $\mathscr{N}_N - \mathscr{N}_S = 2$; and when a node

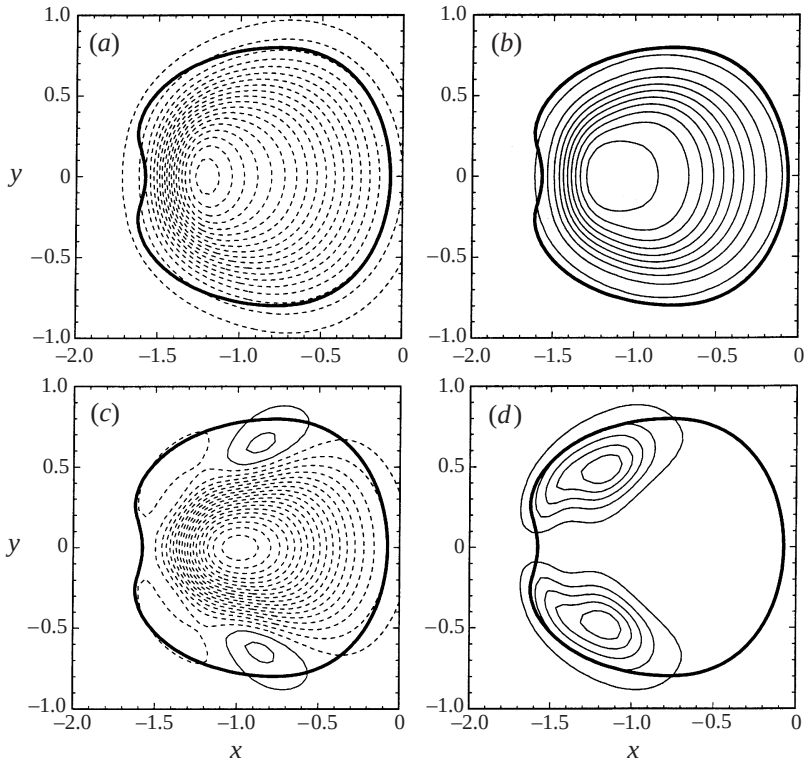

FIGURE 22. Contours on $z = -0.1$ at $t = 7$ of (*a*) ω_y/ω_c (contour increment 0.05); (*b*) $\mathscr{V}_{dy}$ (contour increment 0.05); (*c*) $\mathscr{V}_{sy}$ (contour increment 0.05); and (*d*) $\mathscr{V}_{ty}$ (contour increment 0.05). Solid contours represent positive values while dashed lines represent negative values. The thick line is the contour $\mathscr{C}$ corresponding to $|\omega|/\omega_c = 0.25$ at $z = -0.1$.

or a saddle appears on the boundary of the surface (say the symmetry plane), $\mathscr{N}_N + \frac{1}{2}\mathscr{N}_{N'} - \mathscr{N}_S - \frac{1}{2}\mathscr{N}_{S'} = -1$, where $\mathscr{N}_{N'}$ ($\mathscr{N}_{S'}$) is the number of such boundary nodes (saddles).

Figure 25 plots the streamlines on the free surface for Case II at different stages of the connection. Prior to connection, $t = 3$ (figure 25*a*), there are two stagnation points on the centreline: a sink (N_1) inside the 'down-wash' region where the connection occurs later, and a source (N_2). At an early stage of connection, $t = 5$ (figure 25*b*), N_2 and N_1 both move downstream with the underlying ring but the distance between them is shortening while the sink (N_1) has begun to turn into a saddle. The latter is fully formed at $t = 6$ (figure 25*c*) which shows a saddle (S) with two spirals (N_3) and (N_4) at its two ends. These two spirals lie at the locations of vortex connection on the free surface. At a later stage of the connection process, $t = 7$ (figure 25*d*), the source (N_2) moves toward the saddle (S) and the two begin to merge on the centreline. After the connection, $t = 9$ (figure 25*e*), the singular points on the centreline completely disappear and the two spirals become fully developed. Note that $\mathscr{N}_N - \mathscr{N}_S = 2$ is satisfied at all times.

Figure 26 shows the streamlines in the upper portion of the vertical symmetry plane at the corresponding times. At $t = 3$ (figure 26*a*), there are two (half) saddle points (S_1', S_2') at the free surface on either side of the streamlines of the secondary surface vorticity. At $t = 5$ (figure 26*b*), the top part of the vortex ring reaches the free surface,

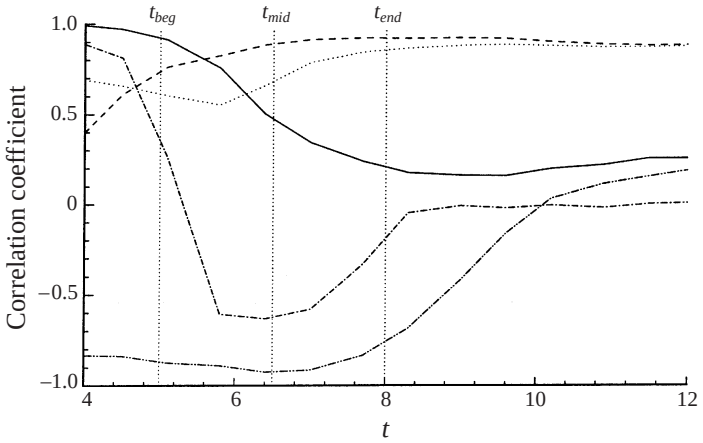

FIGURE 23. Time evolution of correlation coefficients between $D\omega_z/Dt(z=0)$ and vorticity transformation terms: ———, Cor $[\mathscr{V}_{dz}(z=0)]$; – – – –, Cor$[\mathscr{V}_{sz}(z=0)]$; – · – · –, Cor $[\mathscr{V}_{dz}(z=-0.1)]$; · · · · · · · , Cor $[\mathscr{V}_{sz}(z=-0.1)]$; —··—··— , Cor $[\mathscr{V}_{ty}(z=-0.1)]$.

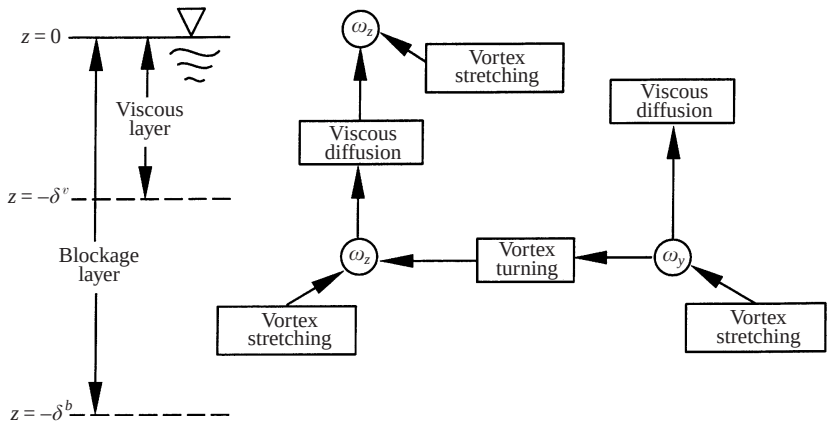

FIGURE 24. A schematic plot of vorticity transformation mechanism near the free surface during connection.

and S_1', S_2' approach each other on the free surface. The presence of the secondary surface vorticity is diminished as is the size of the primary vortex. At $t=6$ (figure 26*c*), neither the primary nor the secondary vorticity can be clearly distinguished. At later times ($t=7,9$) S_1' and S_2' merge and disappear and there is no singular point in this portion of the symmetry plane.

4.3.2. *Connection time and its dependence on F_r, R_e and α*

In the absence of quantitative information regarding the vorticity, Bernal & Kwon (1989) defined the connection time T as the elapsed time from the initial contact of the vortex ring with the free surface to the time when two dimples are first observed as distinct dark spots on the free surface. In addition to the somewhat non-precise definition of the beginning and ending events, a definition of the latter

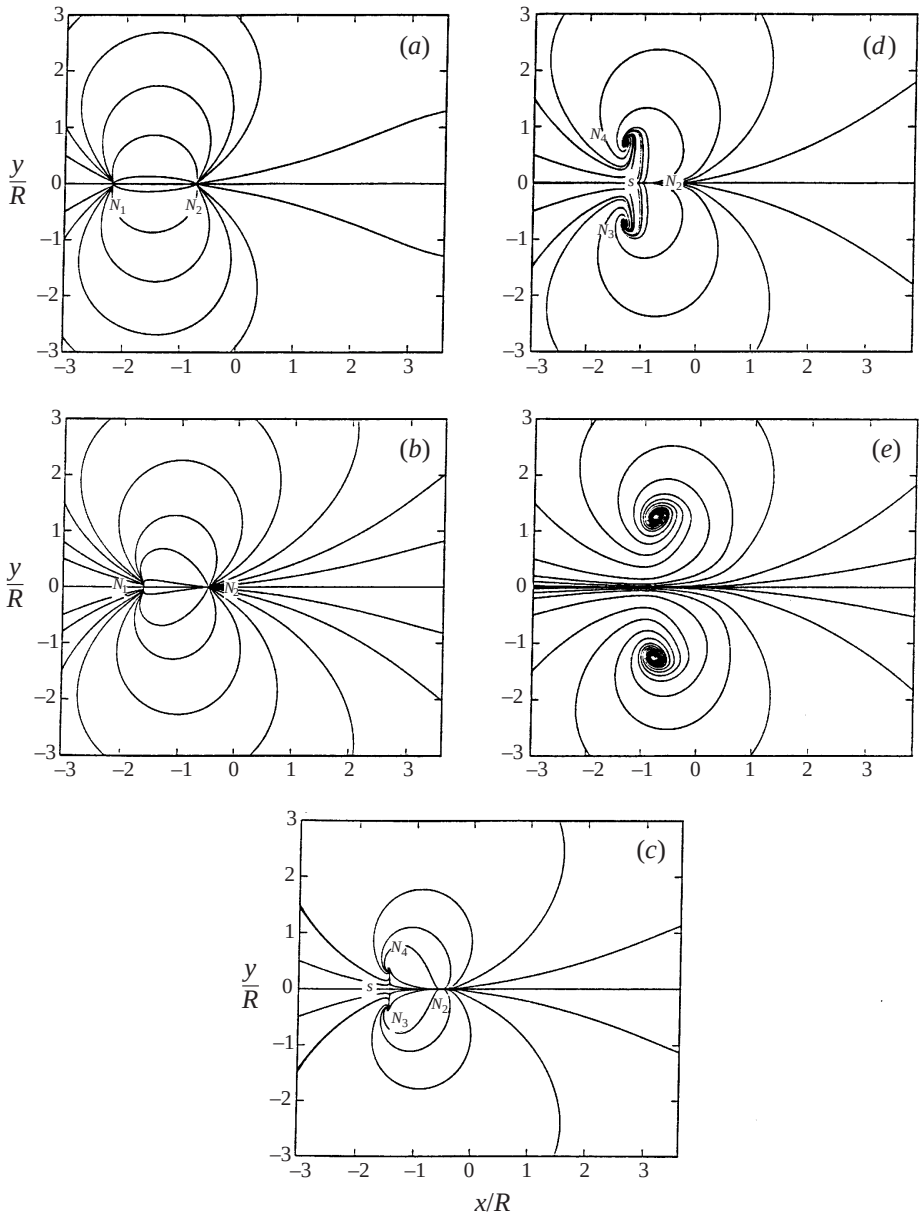

FIGURE 25. Streamlines on the free surface (Case II) at $t =$ (*a*) 3; (*b*) 5; (*c*) 6; (*d*) 7; (*e*) 9.

based on surface elevation features does not, in general, provide direct correlation with evolution of the connected vorticity (cf. figure 8 and Appendix).

If circulation data are available, it is common to define T in terms of the time required for appreciable fractions of the circulations on the relevant (half-)planes to be gained or lost. While this definition provides a useful measure in a global/integrated sense, the definitions of these fractions are necessarily imprecise and, if chosen inappropriately, may obscure the dependence of T on changes in the parameters of the problem.

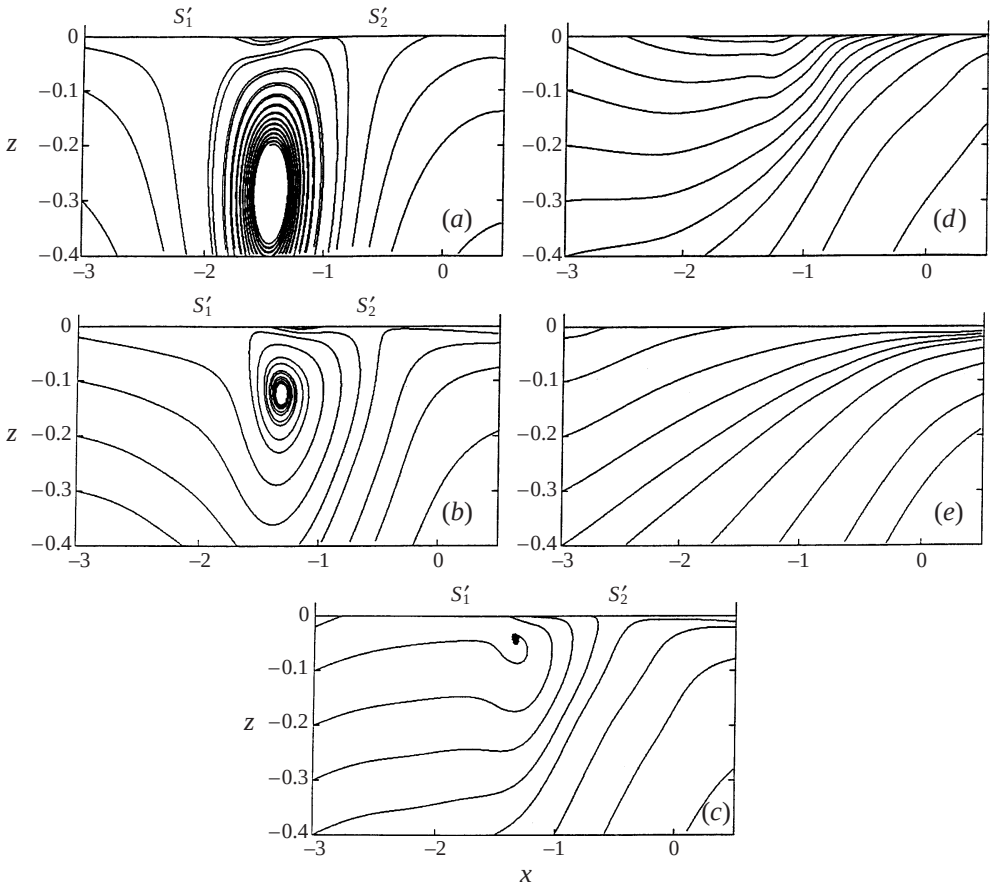

FIGURE 26. Streamlines on the vertical symmetry plane (Case II) at $t =$ (*a*) 3; (*b*) 5; (*c*) 6; (*d*) 7; (*e*) 9.

If the flow topology is known, a useful and objective definition of T can be obtained in terms of the changes of the streamline topology on the free surface. Referring to figure 25, we observe that the vortex connection process is characterized by the appearance and then disappearance of a saddle (S) in the free-surface streamlines. The appearance of the saddle is accompanied by spirals at the two ends which indicate vortices connected there. Thus, the change of the (sink) node (N_1) to a saddle corresponds to the beginning of connection, and the cancellation of the saddle with the (source) node (N_2) to the end of the vortex connection. We therefore define the connection time based on streamline topology, T_ψ, as the elapsed time between the appearance and the disappearance of the saddle. We note that such a definition of connection time can be readily implemented in physical experiments where instantaneous horizontal velocity fields at the free surface are available (say using DPIV).

For comparison, we define a connection time based on velocity circulation, T_Γ, as the elapsed time for Γ_z/Γ_0 on the free surface to increase from 0.2 to 0.75. These fractions are chosen so that T_ψ and T_Γ are approximately the same for the Case II we have been considering so far. The values of T_ψ and T_Γ for the different cases

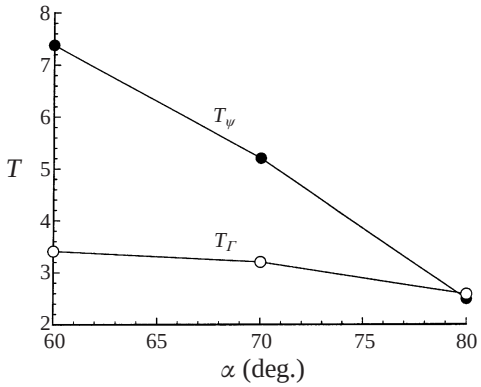

FIGURE 27. Dependence of connection times T_ψ and T_Γ on initial vortex ring incidence angles α.

are given in table 2. Comparing Cases I and II, we see that T_ψ and T_Γ are close for this case regardless of Froude number. Comparing Cases II–IV where (only) α is different, we see that T_ψ and T_Γ differ substantially as α decreases. For the same (small) α, comparing Cases IV–VI, we see that the differences between T_ψ and T_Γ are larger for greater R_e. Overall, it is seen that T_ψ is much more sensitive to changes in the physical parameters, and as a diagnostic, should be more useful than T_Γ for understanding/distinguishing vortex connections under different physical conditions.

From table 2 Cases I and II, we see the free-surface case (Case II) has a somewhat smaller T_ψ relative to the free-slip case (Case I) (the free-surface effect cannot be discerned from T_Γ). That the presence of a free surface decreases connection time can be expected. The vortex connection at a free surface is characterized by the generation of secondary surface vorticity (§4.1), which, being of opposite sign to that of the primary vortex, accelerates the connection process. For this value of F_r, the overall effect is, however, still relatively small.

From table 2 Cases II–IV, we see that there is a strong effect of initial ring incidence angle α on T_ψ (and T_Γ). This dependence is plotted in figure 27. T_ψ increases with decreasing α with a roughly linear dependence in the range of α shown. We observe that T_Γ also increases with decreasing α although the changes are relatively small. This phenomenon that smaller α takes longer for the vortex to connect is consistent with previous studies (e.g. Kida *et al.* 1991).

Finally we examine the influence of Reynolds number by comparing Case IV ($R_e = 1570$), Case V ($R_e = 942$), and Case VI ($R_e = 471$) in table 2. The connection time based on streamline topology shows clearly the decrease of T_ψ with decreasing Reynolds number. Since the connection process is ultimately diffusion controlled, the decrease of connection time with increase of viscosity is expected (e.g. Kambe 1984; Saffman 1990; Shelley *et al.* 1993). Interestingly, this behaviour is not shown in T_Γ which in fact increases somewhat with decreasing R_e.

5. Conclusions

We study, as a canonical example of laminar free-surface vortex connection, the laminar interactions at a free surface when an oblique vortex ring impinges on the surface. We perform numerical simulations of the Navier–Stokes equations with vis-

cous free-surface boundary conditions. The connection process is elucidated in detail by investigating vortex structure, free-surface elevation, surface secondary vorticity, vorticity flux at the free surface, and streamline topology.

A primary objective is to understand the detailed mechanism of the vortex connection. We find that a key to this understanding is the identification of two surface layers near the free surface: an inner viscous layer and an outer blockage layer, which are caused by the dynamic and kinematic free-surface boundary conditions, respectively. The mechanisms of vorticity transformations via turning, stretching, and diffusion take on distinct roles in the surface layers: the dominant mechanism in the blockage layer is that of vortex turning, that in the viscous layer is that of viscous diffusion, while vortex stretching (of primarily the surface-parallel and surface-normal vorticities in the outer and inner layers respectively) is important throughout.

With the availability of the flow field, we apply finally a definition of vortex connection time based on the change in topology of the free-surface streamlines. This definition is precise and objective, and is found to be more useful to quantify the dependence of connection time on the physical parameters compared to a definition based on velocity circulations.

This research was supported by the Office of Naval Research under the program management of Dr E. P. Rood. The authors wish to thank Professor M. Gharib for the experimental results we use for comparison, and for valuable discussions during the course of this study.

Appendix. Relation between elevation and normal vorticity at a free surface

Surface disturbances are often used to infer information regarding the underlying connected vorticity at the surface (e.g. Bernal & Kwon 1989). We show in this Appendix, through two simple examples, that surface vertical vorticity and elevation are not necessarily well correlated.

Assuming steady flow and ignoring viscosity, we have

$$\nabla\left(P+\frac{V^2}{2}+\frac{z}{F_r^2}\right)\equiv\nabla\mathscr{H}=\boldsymbol{V}\times\boldsymbol{\omega},$$

and hence

$$\nabla^2\mathscr{H}=\nabla\cdot(\boldsymbol{V}\times\boldsymbol{\omega}). \tag{A 1}$$

On the free surface, $P=0$, and we solve (A 1) to obtain

$$\eta=F_r^2\left(-\frac{V^2}{2}+\mathscr{H}\right). \tag{A 2}$$

If the vorticity field $\boldsymbol{\omega}$ is (vertically) axisymmetric, it follows from symmetry that η must be also, and hence η and ω_z must be well correlated. We now consider two examples where $\boldsymbol{\omega}$ is not (vertically) axisymmetric: (*a*) a two-dimensional (ω_z only) non-circular vorticity distribution; and (*b*) a three-dimensional vorticity distribution corresponding to an oblique circular cylinder making a 10° angle with the vertical

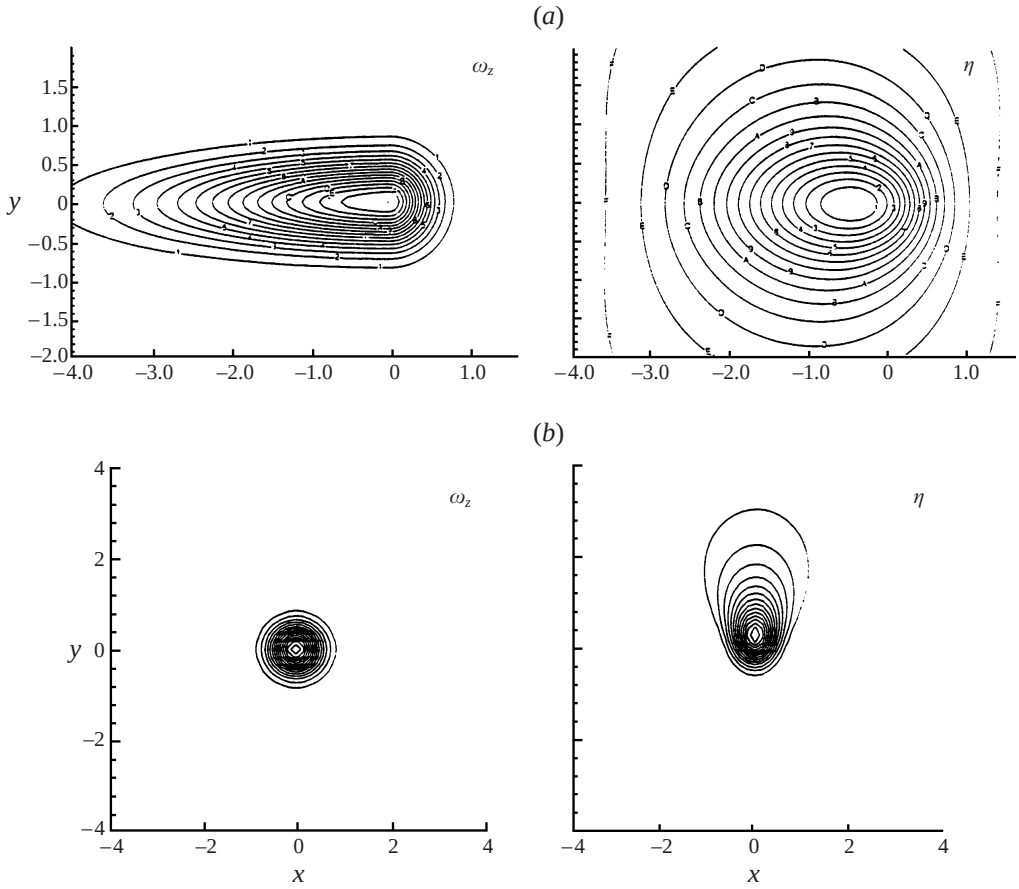

FIGURE 28. Contours of free-surface elevation η and surface-normal vorticity ω_z for examples (*a*) and (*b*).

axis. Solving (A 1) and (A 2), we obtain η corresponding to these vorticity distribution. Figure 28 compares contours of η and ω_z, which show that neither the contour shapes nor maximum positions correspond. Thus a correlation between η and ω_z does not in general obtain.

REFERENCES

BATCHELOR, G. K. 1967 *An Introduction to Fluid Dynamics*. Cambridge University Press.

BERNAL, L. P., HIRSA, A., KWON, J. T. & WILLMARTH, W. W. 1989 On the interaction of vortex rings and pairs with a free surface active agent. *Phys. Fluids* A **1**, 2001–2004.

BERNAL, L. P. & KWON, J. T. 1989 Vortex ring dynamics at a free surface. *Phys. Fluids* A **1**, 449–451.

DOMMERMUTH, D. G. 1993 The laminar interactions of a pair of vortex tubes with a free surface. *J. Fluid Mech.* **246**, 91–115.

DOMMERMUTH, D. G. & Yue, D. K. P. 1990 A numerical study of three-dimensional viscous interactions of vortices with a free surface. *Proc. 18th Symp. Naval Hydrodynamics, Ann Arbor, Michigan*, pp. 727–788. National Academy Press.

GHARIB, M. 1994 Some aspects of near-surface vortices. *Proc. Twelfth US National Congress of Applied Mechanics* (ed. A. S. Kobayashi). *Appl. Mech. Rev.* **47**, S157–S162.

GHARIB, M. & WEIGAND, A. 1996 Experimental study of vortex disconnection and connection at a free surface. *J. Fluid Mech.* **321**, 59–86.

Gharib, M., Weigand, A., Willert, C. & Liepmann, D. 1992 Experimental study of vortex reconnection to a free surface: A physical flow model. *Proc. 19th. Symp. on Naval Hydrodynamics, Seoul, Korea*, pp. 507–520. National Academy Press.

Hunt, J. C. R., Abell, C. J., Peterka, J. A. & Woo, H. 1978 Kinematical studies of the flows around free or surface-mounted obstacles: Applying topology to flow visualization. *J Fluid Mech.* **86**, 179–200.

Kambe, T. 1984 Some dissipation mechanisms in vortex systems. *Turbulence and Chaotic Phenomena in Fluids* (ed. T. Tatsumi), pp. 239–244. Elsevier.

Kasischke, E., Meadows, G. & Jackson, P. 1984 The use of synthetic aperture radar to detect hazards to navigation. *ERIM Rep.* Ann Arbor, Michigan.

Kida, S., Takaoka, M. & Hussain, F. 1991 Collision of two vortex rings. *J. Fluid Mech.* **230**, 583–646.

Lamb, H. 1932 *Hydrodynamics.* Dover.

Longuet-Higgins, M. S. 1998 Vorticity and curvature at a free surface. *J. Fluid Mech.* **356**, 149–153.

Lugt, H. J. 1987 Local flow properties at a viscous free surface. *Phys. Fluids* **30**, 3647–3652.

Lugt, H. J. & Ohring, S. 1994 The oblique rise of a viscous vortex ring toward a deformable free surface. *Meccanica* **29**, 313–329.

Lundgren, T. S. 1988 A free surface vortex method with weak viscous effects. *Mathematical Aspects of Vortex Dynamics* (ed. R. E. Caflish), pp. 68–79. SIAM.

Melander, M. V. & Hussain, F. 1990 Topological aspects of vortex reconnection. In *Topological Fluid Mechanic* (ed. H. K. Moffatt & A. Tsinober), pp. 485–499. Cambridge University Press.

Ohring, S. & Lugt, H. J. 1996 Interaction of an obliquely rising vortex ring with a free surface in a viscous fluid. *Meccanica* **31**, 623–655.

Rood, E. P. 1994*a* Interpreting vortex interactions with a free surface. *Trans. ASME J. Fluids Engng* **116**, 91–94.

Rood, E. P. 1994*b* Myths, math, and physics of free-surface vorticity. *Appl. Mech. Rev.* **47**, S152–S156.

Saffman, P. G. 1990 A model of vortex reconnection. *J. Fluid Mech.* **212**, 395–402.

Sarpkaya, T. 1996 Vorticity, free surface, and surfactants. *An. Rev. Fluid. Mech.* **28**, 83–128.

Sarpkaya, T. & Suthon, P. 1990 Wake of a vortex pair on the free surface. *Proc. 17th Symp. on Naval Hydrodynamics, The Hague*, pp. 53–60. National Academy Press.

Shelley, M. J., Meiron, D. I. & Orszag, S. A. 1993 Dynamical aspects of vortex reconnection of perturbed anti-parallel vortex tubes. *J. Fluid Mech.* **246**, 613–652.

Tsai, W. T. & Yue, D. K. P. 1995 Effects of soluble and insoluble surfactant on laminar interactions of vortical flows with a free surface. *J. Fluid Mech.* **289**, 315–349.

Willert, C. E. & Gharib, M. 1997 The interaction of spatially modulated vortex pairs with free surfaces. *J. Fluid Mech.* **345**, 227–250.

Zhang, C. 1996 Turbulent free-surface wakes behind towed model – experimental measurements, numerical simulations and stability analysis. PhD thesis, Department of Ocean Engineering, MIT.